Rate-independent dissipation in phase-field modelling of displacive transformations[☆]

K. Tůma[a,b], S. Stupkiewicz[a,*], H. Petryk[a]

[a]Institute of Fundamental Technological Research, Polish Academy of Sciences, Pawińskiego 5B, 02-106 Warsaw, Poland
[b]Faculty of Mathematics and Physics, Charles University, Sokolovská 83, 186 75 Prague, Czech Republic

---

Abstract

In this paper, rate-independent dissipation is introduced into the phase-field framework for modelling of displacive transformations, such as martensitic phase transformation and twinning. The finite-strain phase-field model developed recently by the present authors is here extended beyond the limitations of purely viscous dissipation. The variational formulation, in which the evolution problem is formulated as a constrained minimization problem for a global rate-potential, is enhanced by including a mixed-type dissipation potential that combines viscous and rate-independent contributions. Effective computational treatment of the resulting incremental problem of non-smooth optimization is developed by employing the augmented Lagrangian method. It is demonstrated that a single Lagrange multiplier field suffices to handle the dissipation potential vertex and simultaneously to enforce physical constraints on the order parameter. In this way, the initially non-smooth problem of evolution is converted into a smooth stationarity problem. The model is implemented in a finite-element code and applied to solve two- and three-dimensional boundary value problems representative for shape memory alloys.

Keywords: phase-field method, microstructure, martensite, twinning, non-smooth optimization

---

1. Introduction

The key feature of the phase-field method is that the phase interfaces are treated as diffuse and are described by the phase-field variables, usually called the order parameters, that are continuous in space and time. Nucleation, migration and annihilation of interfaces can thus be modelled using a fixed computational grid (or mesh). As a result, the phase-field method is a powerful tool for the modelling of various problems of microstructure evolution (cf. Chen, 2002; Moelans et al., 2008; Steinbach, 2009; Wang and Li, 2010), including those related to martensitic transformations (e.g., Wang and Khachaturyan, 1997; Artemev et al., 2000; Levitas and Preston, 2002; Ahluvalia et al., 2004; Mamivand et al., 2013).

Classical formulations of the phase-field method, as well as the vast majority of its numerous versions and applications, rely on a viscous-type evolution equation for the order parameter so that interface motion is triggered by an arbitrarily small driving force. As a consequence, for a constant external loading, a system governed by a viscous evolution equation asymptotically evolves towards an equilibrium state of vanishing thermodynamic driving forces. While viscous evolution is physically justified in many material systems, rate-independent effects constitute an essential feature of experimentally observed response in displacive transformations, such as martensitic phase transformation and twinning studied here. It is then not appropriate to assume that an arbitrarily small driving force may trigger microstructure evolution, and an evolution law with a finite threshold on the driving force is needed.

Shape memory alloys (Otsuka and Wayman, 1998; Bhattacharya, 2003), which exhibit pseudoelasticity and shape memory effects resulting from martensitic phase transformations, are a prominent example of a

---

[☆] Published in *J. Mech. Phys. Solids*, vol. 114, pp. 117-142, 2018, doi: 10.1016/j.jmps.2018.02.007

[*] Corresponding author. Tel.: (+48) 22 826 12 81 ext. 338.

Email addresses: `ktuma@ippt.pan.pl` (K. Tůma), `sstupkie@ippt.pan.pl` (S. Stupkiewicz), `hpetryk@ippt.pan.pl` (H. Petryk)

class of materials in which the response to a sufficiently slow loading is basically rate-independent, and a cyclic response is characterized by a finite width of a hysteresis loop that does not vanish as the external loading rate tends to zero. Rate-independent dissipation should thus be included in constitutive models of those materials. In fact, a purely rate-independent response is assumed in the majority of those models, both micromechanical (e.g., Šittner and Novák, 2000; Thamburaja and Anand, 2001; Stupkiewicz and Petryk, 2002; Kružík et al., 2005; Hackl and Heinen, 2008) and macroscopic (e.g., Raniecki and Lexcellent, 1994; Auricchio and Taylor, 1997; Souza et al., 1998; Reese and Christ, 2008; Sedlák et al., 2012; Stupkiewicz and Petryk, 2013), see also (Mielke and Roubíček, 2015).

However, purely rate-independent dissipation, as discussed above, is actually not physically justified at small time and length scales at which the phase-field method is used to model microstructure evolution. It is also not convenient for computational treatment of interface migration because even a quasi-static evolution is then not guaranteed, particularly at the instants of formation and annihilation of interfaces. A kinetic relation between the Eshelby driving force and the speed of propagation of an interface was proposed by Abeyaratne and Knowles (1991, 1997) in the form that comprises both a rate-independent threshold value of the driving force and a viscous response above it. Mixed-type dissipation that combines rate-independent and viscous contributions has then been adopted in several models in the context of phase transformations (e.g., Helm and Haupt, 2003; Idesman et al., 2005; Sadjadpour and Bhattacharya, 2007; Roubíček, 2011; Bartel and Menzel, 2016). Viscous effects (leading to rate-dependent dissipation) may be considered, in addition to the primal rate-independent contribution, in order to include the actual physical viscous effects (e.g., Helm and Haupt, 2003) or to regularize purely rate-independent models, which in some formulations are difficult to handle theoretically or numerically (e.g., Sadjadpour and Bhattacharya, 2007). Note that, in shape memory alloys, rate-dependent effects are naturally introduced by thermomechanical couplings due to the latent heat and the related temperature changes and heat conduction, although we are here concerned with isothermal processes only. A more general discussion of the scale-sensitive split of dissipation into rate-independent and rate-dependent parts can be found, e.g., in Petryk (2005) and Petryk and Stupkiewicz (2010), cf. also explicit one-dimensional examples (e.g., Abeyaratne et al., 1996; Ngan and Truskinovsky, 1999; Puglisi and Truskinovsky, 2002).

Despite the importance of both the rate-independent and viscous effects in the modelling of displacive transformations accompanied by microstructure evolution, the present authors are not aware of any general formulation and implementation of the phase-field method that would include rate-independent dissipation. This is done in the present paper, in the case of two-phase microstructures, for the first time. For comparison, motion of a diffuse interface governed by a rate-dependent evolution law with a finite threshold on the driving force has been studied by Levitas et al. (2010) in a one-dimensional setting, however, the model does not admit generalization to two and three dimensions. Phase-field models developed in a different context of rate-independent crack propagation with viscous regularization (e.g., Miehe et al., 2010) are also not directly applicable to martensitic microstructures because (diffuse) fracture is essentially irreversible while microstructure evolution involves nucleation, migration and annihilation of interfaces. At the same time, in general terms, the model developed in this work shares some similarities with that of Miehe et al. (2010). Notably, the incremental variational framework is employed in both cases, however, with several differences, the most important being the non-smooth minimization framework and the subdifferential calculus that are used here along with the computational treatment based on the augmented Lagrangian method.

By performing phase-field simulations, Levitas and Lee (2007) and Levitas et al. (2010) have shown that spatially oscillating stress fields may result in a finite threshold to an overall interface motion, even though locally the interface motion is governed by the classical Ginzburg–Landau equation with purely viscous dissipation. This can actually be considered a kind of scale transition in space and/or in time. While spatially distributed obstacles to interface motion and wiggly energy landscapes indeed correspond to the physical small-scale origin of the rate-independent dissipation (e.g. Abeyaratne et al., 1996; Bhattacharya, 1999; Puglisi and Truskinovsky, 2002), our aim here is to develop a phase-field model that includes the rate-independent dissipation at a higher scale at which those fine features are not (and cannot be) directly resolved.

In this paper, rate-independent dissipation is introduced into the phase-field framework for modelling of displacive transformations by extending our recent finite-strain phase-field model (Tůma et al., 2016; Tůma and Stupkiewicz, 2016). Specifically, the variational formulation, in which the evolution problem is formulated as a constrained minimization problem for a global rate-potential, is extended by including a non-smooth mixed-type dissipation potential that combines the viscous and rate-independent contributions. This is done by using the subdifferential calculus (Rockafellar, 1970; Peypouquet, 2015) to arrive at a concise variational treatment of the rate-independent, non-differentiable but convex part of an overall potential. The implicit backward-Euler scheme is next applied to derive the incremental finite-step problem. Its computational treatment employs the augmented Lagrangian method (cf. Bertsekas, 1996) in the version of Stupkiewicz and Petryk (2013) in which a single Lagrange multiplier field is used to enforce physical constraints on the order parameter and to handle the non-smooth dissipation functional. The initially non-smooth problem of evolution is finally converted into a *smooth* stationarity problem, convenient to be solved numerically. The model is implemented in a finite-element code and applied to solve representative two- and three-dimensional boundary value problems. Coarsening and arrest of a twinned-martensite microstructure in an unconstrained domain is first studied. This example is accompanied by an analytical sharp-interface model of a single interface driven by interfacial energy, and perfect agreement of this model with the corresponding phase-field model is demonstrated. Simulations of compression of a pseudoelastic micro-pillar are also reported along with a detailed analysis of the effect of loading rate on the overall hysteresis.

2. Rate-independent dissipation in phase-field modelling

2.1. Background: viscous dissipation

For introduction, we begin with the classical phase-field approach that includes only viscous dissipation, i.e. without rate-independent dissipation. Suppose for simplicity that there is a single non-conserved order parameter η, for instance, the volume fraction of a product phase. The evolution rule for the order parameter η is defined in terms of the material time derivative $\dot{\eta} = \mathrm{d}\eta/\,\mathrm{d}t$ of η by the basic Ginzburg–Landau equation (cf. Penrose and Fife, 1990; Chen, 2002),

$$\dot{\eta} = Lf\,, \qquad f = -\frac{\delta\mathcal{F}}{\delta\eta}, \tag{1}$$

where $L > 0$ is a constant mobility parameter, f is the thermodynamic driving force, and $\frac{\delta\mathcal{F}}{\delta\eta}$ is the functional derivative of the Helmholtz free energy functional $\mathcal{F}$, to be specified later.

The *actual* dissipation rate density (per unit volume) equals $f\dot{\eta}$ by the definition of f. Following Onsager (1931), by introducing a *quadratic dissipation potential* $D^{\mathrm{v}}(\dot{\eta})$,

$$D^{\mathrm{v}}(\dot{\eta}) = \frac{1}{2L}\dot{\eta}^2, \tag{2}$$

as a potential for a dissipative force conjugate to $\dot{\eta}$, the evolution equation (1) is equivalently written down as the *pointwise* minimization problem, i.e. formulated at a material point:

$$\text{find } \min_{\dot{\eta}\in\mathbb{R}} \left(D^{\mathrm{v}}(\dot{\eta}) - f\dot{\eta}\right). \tag{3}$$

The quadratic dissipation potential $D^{\mathrm{v}}(\dot{\eta})$ is clearly distinct from the *virtual* dissipation rate density $\frac{\mathrm{d}D^{\mathrm{v}}}{\mathrm{d}\dot{\eta}}\dot{\eta}$. For a solution to the equation (1), or equivalently to the minimization problem (3), we have $f = \frac{\mathrm{d}D^{\mathrm{v}}}{\mathrm{d}\dot{\eta}}$ and $f\dot{\eta} = 2D^{\mathrm{v}}(\dot{\eta})$. The motivation to reformulate the pointwise evolution rule (1) as a minimization problem (3) comes from the easy transformation of the latter to a *global* formulation ('global' in the sense of being formulated for the entire body). Indeed, in view of the definition $(1)_2$ of f as a functional derivative of $\mathcal{F}$ and under appropriate boundary conditions, the pointwise minimization problem can be extended to the global minimization of a sum of $\dot{\mathcal{F}}$ and a volume integral of D^{v} with respect to a field of $\dot{\eta}$, cf. Hildebrand and Miehe (2012); Tůma et al. (2016).

Equation (1) does not include rate-independent dissipation; note that the thermodynamic driving force f vanishes as $\dot{\eta} \to 0$ at constant L. It means that the material response tends to a reversible process when the transformation speed tends to zero, which is characterized by a vanishing hysteresis loop upon reverse transformation. On the other hand, in the case of martensitic phase transition in shape memory alloys, it is commonly observed experimentally that the width of a hysteresis loop does not tend to zero no matter how slow the external loading rate is. Therefore, there is a need to enhance the basic equation (1) by including rate-independent dissipation.

2.2. *Background: rate-independent dissipation*

Rate-independent response is introduced by making an assumption different from that in Section 2.1, namely, by neglecting the viscous, rate-dependent dissipation and taking instead the rate-independent one. Accordingly, define a rate-independent dissipation potential $D^{\mathrm{in}}(\dot{\eta})$ that is positively homogeneous of degree one in $\dot{\eta}$, i.e. $D^{\mathrm{in}}(r\dot{\eta}) = rD^{\mathrm{in}}(\dot{\eta})\ \forall r > 0$. In the simplest case,

$$D^{\mathrm{in}}(\dot{\eta}) = f_{\mathrm{c}}\dot{\eta} \qquad \text{for } \dot{\eta} \geq 0\,, \tag{4}$$

with the critical driving force $f_{\mathrm{c}} > 0$ independent of the actual value of $\dot{\eta}$. However, the time derivative $\dot{\eta}$ from now on is to be understood in the *one-sided* sense (for $\mathrm{d}t > 0$), and the value of f_{c} may depend on the sign of $\dot{\eta}$. In the case of the *forward* phase transition, $\dot{\eta} \geq 0$, the related rate-independent phase transformation rule is analogous to that in classical plasticity (cf. Rice, 1975; Stupkiewicz and Petryk, 2002),

$$\dot{\eta} \geq 0\,, \qquad f \leq f_{\mathrm{c}}\,, \qquad (f - f_{\mathrm{c}})\dot{\eta} = 0\,. \tag{5}$$

This rule represents precisely the Kuhn–Tucker conditions for the minimization problem

$$\text{find} \min_{\dot{\eta}\in\mathbb{R}^+} \left(D^{\mathrm{in}}(\dot{\eta}) - f\dot{\eta}\right) \tag{6}$$

analogous to (3), except that D^{v} is replaced with D^{in}.

In the next subsection it is demonstrated how the classical phase-field method (with no inertia effects) can be extended to include the rate-independent dissipation by combining it with the viscous one.

2.3. *Mixed-type dissipation*

Mixed-type dissipation is defined as including both the viscous and rate-independent dissipation types. To include mixed-type dissipation into phase-field modelling, one is tempted, by analogy to formulations (3) and (6), to *assume* minimization of the sum of the respective dissipation potentials as a reasonable trial. It is preferable, however, to begin with a physically based extension of Eq. $(1)_1$ and only then to *derive* the related minimization problem, rather than to assume it at the outset. This is motivated by the fact that the mixed-dissipation potential is no longer a homogeneous function as is the case for each of the potentials (2) and (4) considered separately. It is pointed out that the Onsager principle or any other thermodynamic extremum principle proposed so far for irreversible processes is not universal (see Fischer et al. (2014) for discussion) and requires thus a justification.

The relevant modification of Eq. (1) is most simply explained graphically. Figure 1a shows the invertible (in fact, linear) relationship between f and $\dot{\eta}$ described by Eq. $(1)_1$. Figure 1b shows the multivalued relation between f and $\dot{\eta}$ described by the linear complementarity problem (5) formulated separately for $\dot{\eta}^+ = \dot{\eta} \geq 0$ and for $\dot{\eta}^- = -\dot{\eta} \geq 0$. Figure 1c shows the proposed relation between f and $\dot{\eta}$ obtained by combination of the preceding two. In the special case of a sharp interface model, the relationship of the type shown in Fig. 1c is analogous to the known threshold-type kinetic relation between the Eshelby driving force and the speed of propagation of the interface (cf. Abeyaratne and Knowles, 1991, 1997). A more general nonlinear kinetic relation between f and $\dot{\eta}$, indicated in Fig. 1c by a broken line, can be used for straightforward generalization of the considerations below that are limited for simplicity to the linearized case.

The relation displayed in Fig. 1c by the solid line is described analytically as follows

$$\dot{\eta} = \begin{cases} L\,(f - f_{\mathrm{c}}^{+}) & \text{if } f > f_{\mathrm{c}}^{+} \geq 0, \\ 0 & \text{if } -f_{\mathrm{c}}^{-} \leq f \leq f_{\mathrm{c}}^{+}, \\ L\,(f + f_{\mathrm{c}}^{-}) & \text{if } f < -f_{\mathrm{c}}^{-} \leq 0\,. \end{cases} \tag{7}$$

It is the basic local evolution equation that replaces Eq. $(1)_1$ after including rate-independent dissipation. The mobility L defines here the characteristic time scale of microstructural rearrangements, which is independent of the external time scale related to the loading.

The three cases in Eq. (7) can be written down together in the most compact way as

$$f \in \partial D(\dot{\eta})\,, \tag{8}$$

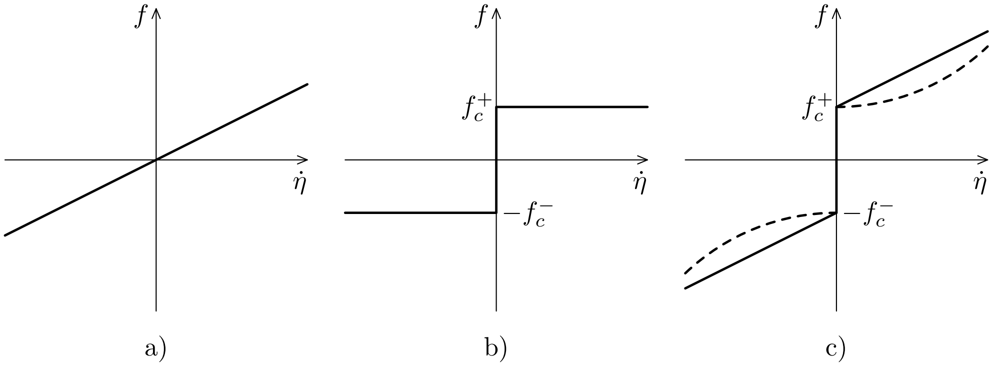

Figure 1: Relation between f and $\dot\eta$ in the case of (a) viscous, (b) rate-independent, and (c) mixed-type dissipation.

by using the concept of a subdifferential ∂D of a non-smooth convex 'dissipation potential' $D(\dot\eta)$ understood now as a pseudo-potential for a dissipative force equal to f. A 'resistance law' of the type of Eq. (8) can be found in the non-smooth mechanics of dissipative systems, cf. Moreau (1970) and many later works (e.g., Moreau, 1974; Halphen and Nguyen, 1975; Raous et al., 1999; Mielke and Roubíček, 2015), frequently in a dual form. The reader is referred to monographs (Rockafellar, 1970; Peypouquet, 2015) for a mathematical background of the subdifferential calculus.

To make the present paper self-contained, it suffices to recall here only the basic definition of a subdifferential $\partial\psi(x)$ of a convex function $\psi:\ \mathbb{R}\to\mathbb{R}\cup\{+\infty\}$ at x as the set of all subgradients x^* of ψ at x that satisfy the subgradient inequality, viz.

$$\partial\psi(x)=\{x^*\in\mathbb{R}\mid \psi(z)\geq\psi(x)+x^*\cdot(z-x)\ \ \forall z\in\mathbb{R}\}\,. \tag{9}$$

Details of the application of this formalism are included below for the clarity of reasoning, although they are mostly elementary from a mathematical point of view. Since we deal with a single order-parameter, we even will not need the (straightforward) extension of Eq. (9) from $\mathbb{R}$ to $\mathbb{R}^n$.

In the present case, fulfilment of Eq. (7) is equivalent to the inclusion (8) with the convex dissipation potential $D(\dot\eta)$ consisting of two convex components,

$$D(\dot\eta)=D^{\rm v}(\dot\eta)+D^{\rm in}(\dot\eta)\,, \tag{10}$$

where the rate-independent component $D^{\rm in}(\dot\eta)$ is defined by

$$D^{\rm in}(\dot\eta)=f_{\rm c}^+\dot\eta^+-f_{\rm c}^-\dot\eta^-\,,\qquad \dot\eta^\pm=\frac{1}{2}(\dot\eta\pm|\dot\eta|)\,,\qquad f_{\rm c}^+\geq 0\,,\ f_{\rm c}^-\geq 0\,. \tag{11}$$

In the special case $f_{\rm c}^-=f_{\rm c}^+=f_{\rm c}$, we obtain $D^{\rm in}(\dot\eta)=f_{\rm c}|\dot\eta|$. This special case of potential (10) was considered in the relevant references cited in the Introduction, but not in the present context of phase-field modelling of martensitic transformations.

To show the equivalence of relations (7) and (8) explicitly, the subdifferential of $D^{\rm in}$ at $\dot\eta$ is identified, by using directly the subgradient inequality, as

$$\partial D^{\rm in}(\dot\eta)=\begin{cases}\{f_{\rm c}^+\} & \text{if } \dot\eta>0,\\ [-f_{\rm c}^-,f_{\rm c}^+] & \text{if } \dot\eta=0,\\ \{-f_{\rm c}^-\} & \text{if } \dot\eta<0.\end{cases} \tag{12}$$

By the addition rule for subdifferentials, in particular when one of the component functions, here $D^{\rm v}$, is differentiable, it follows that $\partial D(0)=[-f_{\rm c}^-,f_{\rm c}^+]$, while for $\dot\eta\neq 0$ the subdifferential $\partial D(\dot\eta)=\{{\rm d}D/{\rm d}\dot\eta\}$ consists of a single element, ${\rm d}D/{\rm d}\dot\eta=\dot\eta/L+f_{\rm c}^+$ for $\dot\eta>0$ or ${\rm d}D/{\rm d}\dot\eta=\dot\eta/L-f_{\rm c}^-$ for $\dot\eta<0$. Relation (8) is thus equivalent to fulfilment of Eq. (7) in every case.

On the other hand, imposing relation (8) is equivalent to the minimization:

$$\text{find } \min_{\dot\eta\in\mathbb{R}} \left(D(\dot\eta) - f\dot\eta\right). \tag{13}$$

The proof follows immediately from Fermat's rule saying that $0 \in \partial\psi(x)$ represents the condition necessary and sufficient for x to be a minimizer of a non-smooth convex function ψ defined over $\mathbb{R}$. Hence, to see the equivalence, it suffices to rewrite relation (8) as

$$0 \in \partial\psi(\dot\eta) \qquad \text{for} \qquad \psi(\dot\eta) = D(\dot\eta) - f\dot\eta\,. \tag{14}$$

2.4. Bound-constrained evolution

If η has the meaning of a volume fraction then the evolution equation in the form (7) or (13) must be accompanied by the physical restriction

$$0 \le \eta \le 1 \qquad \Longrightarrow \qquad (\ \dot\eta \ge 0 \text{ if } \eta = 0 \text{ and } \dot\eta \le 0 \text{ if } \eta = 1\ ). \tag{15}$$

This restriction can be imposed without changing the form of the minimization problem (13). Namely, we note first that the threshold values f_{c}^{+} and f_{c}^{-} can depend in general on the order parameter η. In the subdifferential calculus, the dissipation potential can take the value $+\infty$ in a subdomain, while the product $+\infty \cdot 0 = 0$ by definition. Thus, we can extend the definition of the critical driving forces and introduce $\overline{f}_{\mathrm{c}}^{+}(\eta)$ and $\overline{f}_{\mathrm{c}}^{-}(\eta)$ such that

$$\overline{f}_{\mathrm{c}}^{+}(\eta) = \begin{cases} f_{\mathrm{c}}^{+} & \text{if } \eta < 1, \\ +\infty & \text{otherwise,} \end{cases} \qquad \overline{f}_{\mathrm{c}}^{-}(\eta) = \begin{cases} f_{\mathrm{c}}^{-} & \text{if } \eta > 0, \\ +\infty & \text{otherwise,} \end{cases} \tag{16}$$

and redefine the convex dissipation potentials $\overline{D}^{\mathrm{in}}$ and $\overline{D}$ accordingly, cf. Eqs. (10) and (11),

$$\overline{D}(\dot\eta) = D^{\mathrm{v}}(\dot\eta) + \overline{D}^{\mathrm{in}}(\dot\eta), \qquad \overline{D}^{\mathrm{in}}(\dot\eta) = \overline{f}_{\mathrm{c}}^{+}\dot\eta^{+} - \overline{f}_{\mathrm{c}}^{-}\dot\eta^{-}. \tag{17}$$

It is easy to verify that $\dot\eta$ determined from the new minimization problem

$$\text{find } \min_{\dot\eta\in\mathbb{R}} \left(\overline{D}(\dot\eta) - f\dot\eta\right) \tag{18}$$

cannot take a positive value at $\eta = 1$ or a negative value at $\eta = 0$. Hence, a solution to the minimization problem (18) for the extended definition of $\overline{D}(\dot\eta)$ satisfies not only the original constitutive relation (7) but also the bound constraint (15) imposed on $\dot\eta$. As in the unconstrained case, the solution to the convex minimization problem (18) can be compactly written in the form of the inclusion

$$f \in \partial\overline{D}(\dot\eta) \tag{19}$$

analogous to that in Eq. (8), except that here $\partial\overline{D}(\dot\eta) = \emptyset$ if $\eta \notin [0,1]$. Recall that the *one-sided* time derivative $\dot\eta = \mathrm{d}\eta/\,\mathrm{d}t^{+}$ is used.

Consequently, if the forward rate $\dot\eta$ is determined at every instant from the minimization problem (18) then η, assumed to vary continuously in time, always remains in the interval $[0,1]$ when it starts from an initial value within this interval. When the problem is discretized in time then the physical bounds $0 \le \eta \le 1$ can be imposed on η in a more direct way, as it will be done in Section 2.7.

2.5. Free energy functional

The right-hand expression in Eq. (1) is the classical functional derivative defined by

$$\frac{\delta\mathcal{F}}{\delta\eta} = \frac{\partial F}{\partial\eta} - \nabla\cdot\frac{\partial F}{\partial\nabla\eta}\,, \tag{20}$$

where the Helmholtz free energy functional $\mathcal{F}$ is defined as an integral over a body domain $B \subset \mathbb{R}^3$ in a reference configuration,

$$\mathcal{F}[\mathbf{u}, \eta] = \int_B F(\nabla \mathbf{u}, \eta, \nabla \eta) \, \mathrm{d}\mathbf{X}, \tag{21}$$

of a free energy density F that depends on displacement gradient $\nabla \mathbf{u}$ and on both the order parameter η and its gradient $\nabla \eta$. The gradient $\nabla(\cdot)$ is defined with respect to placement $\mathbf{X}$ in the stress-free reference configuration of the homogeneous parent phase. To simplify the notation, the same symbol is used for a function of $\mathbf{X}$ and its value at $\mathbf{X}$, while the distinction is visualized by square brackets used to denote the functional arguments being functions. The free energy density F is split into the bulk part F_B and the interfacial part F_Γ, i.e.

$$F(\nabla \mathbf{u}, \eta, \nabla \eta) = F_\mathrm{B}(\nabla \mathbf{u}, \eta) + F_\Gamma(\eta, \nabla \eta). \tag{22}$$

The double-obstacle potential (cf. Steinbach, 2009) is adopted here for the interfacial free energy density F_Γ,

$$F_\Gamma(\eta, \nabla \eta) = \gamma \left(\frac{4\ell}{\pi} |\nabla \eta|^2 + \frac{4}{\pi \ell} \eta (1 - \eta) \right), \tag{23}$$

where $\ell > 0$ is the interface thickness parameter that defines the related characteristic length scale which is typically much smaller than the characteristic spatial dimension of the problem. It is shown in Appendix A that for the equilibrium profile of the interface, i.e. when the influence of F_B is neglected and the interface profile is obtained by minimizing the interfacial energy alone, the thickness of the diffuse interface is equal to $\pi \ell$. Furthermore, the scaling factors in Eq. (23) are chosen such that γ is the interfacial energy density per unit reference area.

Note that the double-obstacle potential (23) must be accompanied by the bound constraints (15) on η because $F_\Gamma \to -\infty$ for $\eta \to \pm\infty$. This is crucial here in contrast to the popular double-well potential which is a smooth fourth-order polynomial in η of the form $\eta^2(1 - \eta)^2$ (cf. Steinbach, 2009). In the latter case, violation of the bound constraints is penalized by the potential itself so that they are satisfied approximately without additional treatment.

By the standard multiplicative decomposition, the deformation gradient $\mathbf{F} = \mathbf{I} + \nabla \mathbf{u}$ is split into the elastic part $\mathbf{F}_\mathrm{e}$ and transformation part $\mathbf{F}_\mathrm{t}$, thus $\mathbf{F} = \mathbf{F}_\mathrm{e} \mathbf{F}_\mathrm{t}$, where $\mathbf{F}_\mathrm{t}$ defines a *local* unstressed configuration and $\mathbf{I}$ is the second-order identity tensor.

In this paper, only two-phase microstructures are considered so that only one order parameter is used in the model. Note that multi-phase-field models are readily available (e.g. Steinbach et al., 1996; Wang and Khachaturyan, 1997; Levitas and Preston, 2002), which are, however, based on the viscous-type evolution laws. For the clarity of the paper, the presentation is here deliberately limited to a single order parameter.

The two phases involved are indexed by $i = 1, 2$, and each phase is characterized by the corresponding Bain stretch tensor $\mathbf{U}_i$ and elastic stiffness tensor $\mathbf{L}_i$. The bulk free energy F_B of the mixture is then defined by

$$F_\mathrm{B}(\nabla \mathbf{u}, \eta) = (1 - \eta) F_1^0 + \eta F_2^0 + \frac{1}{2} (\det \mathbf{F}_\mathrm{t}) \, \mathbf{E}_\mathrm{e} \cdot \mathbf{L} \, \mathbf{E}_\mathrm{e} \,, \tag{24}$$

where $\mathbf{E}_\mathrm{e} = \frac{1}{2}(\mathbf{F}_\mathrm{e}^\mathrm{T} \mathbf{F}_\mathrm{e} - \mathbf{I})$ is the elastic Green strain tensor for the mixture, $\mathbf{F}_\mathrm{t}$ is defined by the *logarithmic* mixing rule (Tůma et al., 2016),

$$\mathbf{F}_\mathrm{t}(\eta) = \exp((1 - \eta) \log \mathbf{U}_1 + \eta \log \mathbf{U}_2) \,, \tag{25}$$

the elastic stiffness tensor $\mathbf{L}$ is specified by a Voigt-like rule (applied componentwise),

$$\mathbf{L}(\eta) = (1 - \eta) \mathbf{L}_1 + \eta \mathbf{L}_2 \,, \tag{26}$$

and F_i^0, called the chemical energy, denotes the free energy of i-th phase in a stress-free state. For $\eta = 0$ or $\eta = 1$, the bulk energy F_B specified by Eq. (24) reduces to the free energy of a single phase, $F_i(\nabla \mathbf{u}) = F_i^0 + \frac{1}{2}(\det \mathbf{U}_i) \mathbf{E}_\mathrm{e} \cdot \mathbf{L}_i \mathbf{E}_\mathrm{e}$. For more details, including the justification of the logarithmic mixing rule (25) and references to alternative finite-strain models, see Tůma et al. (2016).

The bulk free energy F_B of the mixture, Eq. (24), has been obtained by adequate averaging of the eigenstrain and elastic moduli tensors, as described above. An alternative class of models can be obtained by applying one of the available homogenization schemes, for instance, the Voigt scheme or the Reuss scheme (Ammar et al., 2009). Particularly appealing is the lamination mixing (Mosler et al., 2014; Schneider et al., 2015) in which the interfacial jump conditions are satisfied within the diffuse interface that is treated as a laminate of variable composition. However, the implementation of this model is not trivial because the lamination orientation is defined by the gradient of the order parameter which is not defined outside the interface. We stress that the choice of the specific form of the bulk free energy F_B does not influence the subsequent developments, and any of the models discussed above can be combined with the mixed-type dissipation, as pursued below.

2.6. Global variational formulation of the rate-problem

In this section, the phase-field problem is formulated as a variational principle in a global sense, i.e. for a body domain B. The transformation of the pointwise minimization problem (13) to a global (integral) formulation follows a route analogous to that in the papers by Hildebrand and Miehe (2012) and Tůma et al. (2016), where, however, no rate-independent dissipation was included. The distinction is that here the dissipation potential is no longer smooth, therefore the variational condition for a minimum with respect to the order parameter is different.

The way of including the equilibrium and boundary conditions is fully analogous and is thus presented here only in outline; the reader is referred to Tůma et al. (2016) for more details. In the phase-field problem at hand, the equation of mechanical equilibrium with the displacement field $\mathbf{u}$ as the basic unknown is coupled with the evolution equation (7) for the field of order parameter η. The global potential energy functional $\mathcal{E}$ of the fields of displacement $\mathbf{u}$ and order parameter η is defined as a sum of the free energy $\mathcal{F}$ and potential energy Ω of external loads, assumed conservative, thus

$$\mathcal{E}[\mathbf{u},\eta]=\mathcal{F}[\mathbf{u},\eta]+\Omega[\mathbf{u}]\,. \tag{27}$$

The unknown fields $(\mathbf{u},\eta)$ change with time t and are influenced by time-dependent boundary conditions, while time t is omitted as a parameter to simplify the notation. The inertia effects are neglected, and thus the evolution problem is considered to be quasi-static.

The condition of *mechanical equilibrium* at each instant can be expressed in a weak form as stationarity of the forward rate $\dot{\mathcal{E}}$ of the potential (27) with respect to arbitrary kinematically admissible variations $\delta\dot{\mathbf{u}}$ of velocities $\dot{\mathbf{u}}$,

$$\delta_{\dot{\mathbf{u}}}\dot{\mathcal{E}}[\dot{\mathbf{u}},\dot{\eta};\mathbf{u},\eta]=0 \qquad \forall\,\delta\dot{\mathbf{u}}\ \text{ such that } \dot{\mathbf{u}},\dot{\mathbf{u}}+\delta\dot{\mathbf{u}}\in\mathcal{V}_{\dot{\mathbf{u}}}=\{\dot{\mathbf{u}}\in\mathcal{W}_{\dot{\mathbf{u}}}\mid\dot{\mathbf{u}}=\dot{\bar{\mathbf{u}}}\text{ on }\partial B_u\}\,, \tag{28}$$

where ∂B_u is the closed part of the boundary of B where the Dirichlet boundary condition for the time-dependent displacement $\mathbf{u}=\bar{\mathbf{u}}(t)$ is prescribed, and $\mathcal{W}_{\dot{\mathbf{u}}}$ is a suitable space of three-dimensional vector functions over (the closure of) B. Since $\dot{\mathcal{E}}$ is, by the chain rule, a linear functional of $(\dot{\mathbf{u}},\dot{\eta})$ and hence $\delta_{\dot{\mathbf{u}}}\dot{\mathcal{E}}[\dot{\mathbf{u}},\dot{\eta};\mathbf{u},\eta]$ does not depend on $\dot{\mathbf{u}}$, the variational equality (28) imposes the equilibrium condition on the displacement field $\mathbf{u}$ rather than on the velocity field $\dot{\mathbf{u}}$; see Tůma et al. (2016) for details.

Before proceeding to the variational formulation, the boundary condition must be specified for the order parameter η whose evolution is locally governed by the pointwise minimization problem (13). For simplicity, it is assumed that η satisfies at each instant the zero Neumann boundary condition over the whole boundary ∂B

$$\frac{\partial F}{\partial\nabla\eta}\cdot\mathbf{n}=0\quad\text{over }\partial B\,, \tag{29}$$

while the Dirichlet boundary conditions can be introduced in a standard manner if needed.

The global rate-potential Π is now introduced in a given state $(\mathbf{u},\eta)$ as

$$\Pi[\dot{\mathbf{u}},\dot{\eta};\mathbf{u},\eta]=\Pi^\mathrm{v}[\dot{\mathbf{u}},\dot{\eta};\mathbf{u},\eta]+\overline{\mathcal{D}}^\mathrm{in}[\dot{\eta}]\,, \tag{30}$$

where Π^v is the rate-dependent part of the potential as in Hildebrand and Miehe (2012) and Tůma et al. (2016),

$$\Pi^\mathrm{v}[\dot{\mathbf{u}},\dot{\eta};\mathbf{u},\eta]=\dot{\mathcal{E}}[\dot{\mathbf{u}},\dot{\eta};\mathbf{u},\eta]+\mathcal{D}^\mathrm{v}[\dot{\eta}]\,,\quad \mathcal{D}^\mathrm{v}[\dot{\eta}]=\int_B D^\mathrm{v}(\dot{\eta})\,\mathrm{d}\mathbf{X}\,, \tag{31}$$

and $\overline{\mathcal{D}}^{\rm in}$ is the rate-independent part of the global dissipation potential,

$$\overline{\mathcal{D}}^{\rm in}[\dot{\eta}] = \int_B \overline{D}^{\rm in}(\dot{\eta})\,{\rm d}\mathbf{X}\,. \tag{32}$$

While the functional $\Pi^{\rm v}$ is smooth (i.e. Gateaux differentiable) with respect to admissible spatial fields $\dot{\mathbf{u}}(\cdot)$ and $\dot{\eta}(\cdot)$, the functional $\overline{\mathcal{D}}^{\rm in}$ is non-smooth, i.e. it is not Gateaux differentiable with respect to $\dot{\eta}(\cdot)$ for $\dot{\eta} = 0$ over a subdomain of non-zero volume. Moreover, $\overline{\mathcal{D}}^{\rm in}$ incorporates the physical constraint $0 \leq \eta \leq 1$ by using the extended definition (16) of the critical driving forces, as discussed in Section 2.4.

The complete quasi-static evolution problem, given by the equations (7) and (28) subject to the boundary conditions (29) and $\dot{\mathbf{u}} = \dot{\bar{\mathbf{u}}}$ on ∂B_u , and starting from an admissible initial state at $t = t_0$, is now formulated as the following minimization problem over suitable function classes $\mathcal{V}_{\dot{\mathbf{u}}}$ and $\mathcal{W}_{\dot{\eta}}$ such that an infimum, if finite, is actually attained:

$$\forall t > t_0 \text{ find } \min_{\dot{\mathbf{u}}\in\mathcal{V}_{\dot{\mathbf{u}}},\dot{\eta}\in\mathcal{W}_{\dot{\eta}}} \Pi[\dot{\mathbf{u}},\dot{\eta};\mathbf{u},\eta]\,. \tag{33}$$

In the special case of spatially discretized, finite-element setting, for prescribed basis functions of class C^0 and piecewise C^1, the solution to problem (33) is searched in a finite dimensional space of continuous and piecewise continuously differentiable functions of the selected form.

The above minimization problem under the assumptions introduced above represents a global variational formulation of the original problem specified by the evolution equation (7) and the standard equilibrium equations along with the assumed boundary conditions and bound constraints imposed on the order parameter. The *proof* follows from the statements (i), (ii) and (iii) below, proven by combining the assumptions and formulae given above. In particular, on account of Eqs. $(1)_2$ and (20), the term dependent on $\nabla\dot{\eta}$ in $\dot{\mathcal{E}}[\dot{\mathbf{u}},\dot{\eta};\mathbf{u},\eta]$ can be transformed by applying the Green theorem, and the boundary integral that appears after this operation vanishes identically on account of Eq. (29). This yields the following expression for the minimized functional Π:

$$\Pi[\dot{\mathbf{u}},\dot{\eta};\mathbf{u},\eta] = \int_B \big(\mathbf{S}\cdot\nabla\dot{\mathbf{u}} - f\dot{\eta} + \overline{D}(\dot{\eta})\big)\,{\rm d}\mathbf{X} + \dot{\Omega}[\dot{\mathbf{u}};\mathbf{u}]\,, \tag{34}$$

where $\mathbf{S} = \mathbf{S}(\nabla\mathbf{u},\eta) = \partial F/\partial\nabla\mathbf{u}$ is the first Piola–Kirchhoff stress. It follows that:

(i) Minimization of Π with respect to $\dot{\mathbf{u}} \in \mathcal{V}_{\dot{\mathbf{u}}}$ reduces to the stationarity condition (28) for $\dot{\mathcal{E}}$ as a linear functional of $\dot{\mathbf{u}}$. In turn, the variational equality (28) is equivalent to the standard weak formulation of equilibrium equations for displacements $\mathbf{u}$ under conservative forces of the potential Ω, both in B and on the boundary $\partial B \setminus \partial B_u$, cf. Tůma et al. (2016).

(ii) Minimization of Π given by Eq. (34) with respect to $\dot{\eta} \in \mathcal{W}_{\dot{\eta}}$ reduces clearly to the pointwise minimization (18) performed almost everywhere (a.e.) in B (i.e., possibly except in a subset of zero volume only).

(iii) Solving the pointwise minimization problem (18) is equivalent to satisfying the inclusion (19) which in turn is equivalent to fulfilment of both the evolution equation (7) and the restrictions (15).

Remark 1. By reversing the line of arguments (i)-(iii) it is apparent that the global minimization problem (33) with respect to $\dot{\eta}$-field is here derived rather than assumed *a priori*. In view of the form of the pointwise minimization (13) involved, this minimum principle can be regarded as an extended, non-smooth version of the Onsager thermodynamic extremal principle, whose classical regular form was recently revisited by Fischer et al. (2014). An attempt to use instead another, even more popular principle of maximum dissipation rate (Ziegler, 1963), fails here in transition to the global dissipation function subject to a single side condition, on account of inhomogeneity of the composite function $D(\dot{\eta})$.

2.7. Implicit time integration scheme

The rate-minimization problem (33) is now discretized in time. The whole time interval $[t_0, T]$ is split into N time steps $t_0 < t_1 < \cdots < t_{N-1} < t_N = T$, where the time increment under consideration is equal to $\tau = \tau_{n+1} = t_{n+1} - t_n$. In the incremental scheme, the previous solution at instant t_n is known, and the corresponding fields are denoted by $(\mathbf{u}_n, \eta_n)$. The subscript $n+1$ referring to the current time instant t_{n+1} is henceforward omitted to make the notation shorter, so that the unknown fields at t_{n+1} are denoted by $(\mathbf{u}, \eta)$ and their rates by $(\dot{\mathbf{u}}, \dot{\eta})$.

As $\dot{\mathcal{E}}$ depends linearly on $(\dot{\mathbf{u}}, \dot{\eta})$, the rate-potential at t_{n+1} can be approximated by applying the implicit backward-Euler scheme as follows,

$$\begin{aligned}\Pi[\dot{\mathbf{u}}, \dot{\eta}; \mathbf{u}, \eta] &= \dot{\mathcal{E}}[\dot{\mathbf{u}}, \dot{\eta}; \mathbf{u}, \eta] + \mathcal{D}^{\mathrm{v}}[\dot{\eta}] + \overline{\mathcal{D}}^{\mathrm{in}}[\dot{\eta}] \\ &\approx \frac{1}{\tau}(\mathcal{E}[\mathbf{u}, \eta] - \mathcal{E}[\mathbf{u}_n, \eta_n]) + \mathcal{D}^{\mathrm{v}}[(\eta - \eta_n)/\tau] + \mathcal{D}^{\mathrm{in}}[(\eta - \eta_n)/\tau] + \mathcal{I}[\eta], \end{aligned} \tag{35}$$

where the bound constraints on η are now enforced explicitly using the indicator function $I_{[0,1]}(\eta)$, viz.

$$\mathcal{I}[\eta] = \int_B I_{[0,1]}(\eta)\,\mathrm{d}\mathbf{X}, \qquad I_{[0,1]}(\eta) = \begin{cases} 0 & \text{if } 0 \leq \eta \leq 1, \\ +\infty & \text{otherwise.} \end{cases} \tag{36}$$

Since $D^{\mathrm{in}}(\dot{\eta})$ is a positively homogeneous function of degree one, we have $\mathcal{D}^{\mathrm{in}}[(\eta - \eta_n)/\tau] = \mathcal{D}^{\mathrm{in}}[(\eta - \eta_n)]/\tau$. The incremental potential Π_τ, as the approximation of $\tau\Pi$ dependent on the unknown fields of $(\mathbf{u}, \eta)$ at the end of the time increment τ, is thus defined through

$$\Pi_\tau[\mathbf{u}, \eta] = \underbrace{\mathcal{E}[\mathbf{u}, \eta] - \mathcal{E}[\mathbf{u}_n, \eta_n] + \tau\mathcal{D}^{\mathrm{v}}[(\eta - \eta_n)/\tau]}_{\Pi_\tau^{\mathrm{v}}[\mathbf{u}, \eta]} + \underbrace{\mathcal{D}^{\mathrm{in}}[\eta - \eta_n] + \mathcal{I}[\eta]}_{\overline{\mathcal{D}}_\tau^{\mathrm{in}}[\eta]}\,. \tag{37}$$

The first underbraced part $\Pi_\tau^{\mathrm{v}}[\mathbf{u}, \eta]$ of the incremental potential is smooth. The last two terms forming the extended rate-independent dissipation term $\overline{\mathcal{D}}_\tau^{\mathrm{in}}$,

$$\overline{\mathcal{D}}_\tau^{\mathrm{in}}[\eta] = \int_B \overline{D}_\tau^{\mathrm{in}}(\eta)\,\mathrm{d}\mathbf{X}, \qquad \overline{D}_\tau^{\mathrm{in}}(\eta) = D^{\mathrm{in}}(\eta - \eta_n) + I_{[0,1]}(\eta)\,, \tag{38}$$

are non-smooth and are responsible for the basic rate-independent part of dissipation and for imposing the physical constraints $0 \leq \eta \leq 1$. Note that $\overline{D}_\tau^{\mathrm{in}} : \mathbb{R} \to \mathbb{R} \cup \{+\infty\}$ is convex.

The minimization (33) of the rate-potential Π is now replaced with minimization of the approximate potential Π_τ performed with respect to $(\mathbf{u}, \eta)$ fields,

$$\text{find } \min_{\mathbf{u} \in \mathcal{V}_{\mathbf{u}}} \min_{\eta \in \mathcal{W}_\eta} \Pi_\tau[\mathbf{u}, \eta], \tag{39}$$

where $\mathcal{V}_{\mathbf{u}} = \{\mathbf{u} \in \mathcal{W}_{\mathbf{u}} \,|\, \mathbf{u} = \bar{\mathbf{u}}(t_{n+1}) \text{ on } \partial B_u\}$. Here, $\mathcal{W}_{\mathbf{u}}$ and $\mathcal{W}_\eta$ are suitable spaces of displacement and order parameter fields, respectively, in which the infimum is actually attained.

In contrast to the minimization problem (33) with respect to the rates $(\dot{\mathbf{u}}, \dot{\eta})$ derived as a weak formulation of (and hence in principle equivalent to) the original problem specified by the assumed governing equations, the above variational formulation for finite increments requires additional arguments. The justification (or derivation, depending on the order of arguments) of the minimization problem (39) runs as follows.

First, solving the minimization problem (39) with respect to $\mathbf{u} \in \mathcal{V}_{\mathbf{u}}$ for any given $\eta \in \mathcal{W}_\eta$ reduces, for the problems examined here, to finding a stationarity point of $\mathcal{E}[\cdot, \eta]$, which represents the standard weak formulation of the equilibrium equations, here at t_{n+1}. In fact, the remaining components of Π_τ do not depend on the displacement field $\mathbf{u}$, so that stationarity of $\mathcal{E}[\cdot, \eta]$ is necessary for the minimum of $\Pi_\tau[\cdot, \eta]$ on account of the smooth dependence of $\mathcal{E}$ on $\mathbf{u} \in \mathcal{V}_{\mathbf{u}}$. The stationarity is also sufficient for the minimum in case of convexity of $\mathcal{E}[\cdot, \eta]$, which we assume as granted to exclude from considerations the cases of purely elastic instability.

Second, the minimization (39) works when the non-smooth term $\overline{\mathcal{D}}_\tau^{\mathrm{in}}[\eta]$ is disregarded, i.e. for an unconstrained viscous evolution problem governed by a smooth potential $\Pi_\tau^{\mathrm{v}}[\mathbf{u}, \eta]$ only. The weak variation of $\Pi_\tau^{\mathrm{v}}[\mathbf{u}, \eta]$ with respect to $\eta \in \mathcal{W}_\eta$ at a fixed $\mathbf{u} \in \mathcal{V}_{\mathbf{u}}$, i.e. the Gateaux differential of $\Pi_\tau^{\mathrm{v}}[\mathbf{u}, \cdot]$ in any direction $\delta\eta \in \mathcal{W}_\eta$, reads

$$\delta_\eta \Pi_\tau^{\mathrm{v}}[\mathbf{u}, \eta] = \int_B \left(\frac{\partial F(\nabla\mathbf{u}, \eta, \nabla\eta)}{\partial\eta}\delta\eta + \frac{\partial F(\nabla\mathbf{u}, \eta, \nabla\eta)}{\partial\nabla\eta} \cdot \nabla\delta\eta + \tau\frac{\partial D^{\mathrm{v}}((\eta - \eta_n)/\tau)}{\partial\eta}\delta\eta \right) \mathrm{d}\mathbf{X}\,. \tag{40}$$

On applying the Green theorem to the second integrand term, the resulting boundary integral vanishes identically on account of Eq. (29). Hence, by denoting the local incremental viscous dissipation potential as

$$D^{\mathrm{v}}_{\tau}(\eta) = \tau D^{\mathrm{v}}((\eta - \eta_n)/\tau) \tag{41}$$

and using Eqs. $(1)_2$, (20) and (41), we obtain

$$\delta_\eta \Pi^{\mathrm{v}}_{\tau}[\mathbf{u}, \eta] = \int_B \left(-f(\nabla\mathbf{u}, \eta, \nabla\eta) + \frac{\partial D^{\mathrm{v}}_{\tau}(\eta)}{\partial \eta} \right) \delta\eta \, \mathrm{d}\mathbf{X} \,. \tag{42}$$

Solving the variational equality $\delta_\eta \Pi^{\mathrm{v}}_{\tau}[\mathbf{u}, \eta] = 0 \; \forall \delta\eta$ is thus equivalent to fulfilment of the viscous evolution equation $(1)_1$ a.e. in B at t_{n+1} under the approximation $\dot{\eta}|_{t_{n+1}} = \frac{\eta - \eta_n}{\tau}$. This is also implied for a solution to the minimization problem (39) in the absence of the non-smooth term $\overline{\mathcal{D}}^{\mathrm{in}}_{\tau}[\eta]$. The converse implication is not immediate since $\Pi^{\mathrm{v}}_{\tau}[\mathbf{u}, \cdot]$ is generally non-convex. However, conditional convexity of $\Pi^{\mathrm{v}}_{\tau}[\mathbf{u}, \cdot]$ in $\mathcal{W}_\eta$ is proven in Appendix B for τ sufficiently small, which is important for reducing problem (39) to that of convex minimization.

Third, when the entire functional $\Pi_\tau[\mathbf{u}, \cdot]$ is examined including its non-smooth part $\overline{\mathcal{D}}^{\mathrm{in}}$ then the usual concept of a derivative is insufficient. The *one-sided* directional derivative of functional $\Pi_\tau[\mathbf{u}, \cdot]$ in the direction of $\delta\eta \in \mathcal{W}_\eta$ at a fixed $\mathbf{u} \in \mathcal{V}_{\mathbf{u}}$ reads

$$\delta^+_\eta \Pi_\tau[\mathbf{u}, \eta] = \lim_{r \to 0^+} \frac{\Pi_\tau[\mathbf{u}, \eta + r\delta\eta] - \Pi_\tau[\mathbf{u}, \eta]}{r} \,. \tag{43}$$

The conditions necessary for $\eta \in \mathcal{W}_\eta$ to be a minimizer of $\Pi_\tau[\mathbf{u}, \cdot]$ at a fixed $\mathbf{u} \in \mathcal{V}_{\mathbf{u}}$ are that $\Pi_\tau[\mathbf{u}, \eta]$ is finite and

$$\delta^+_\eta \Pi_\tau[\mathbf{u}, \eta] \geq 0 \quad \forall \delta\eta \in \mathcal{W}_\eta \,. \tag{44}$$

Using the integral representation of the directional derivative (42) and the integral form (38) of $\overline{\mathcal{D}}^{\mathrm{in}}_{\tau}$, the above conditions, necessary for a minimum of the functional $\Pi_\tau[\mathbf{u}, \cdot]$ that consist of two parts defined by Eq. (37), reduce to the following two pointwise conditions to be satisfied a.e. in B:

$$\eta \in [0, 1] \qquad \text{and} \qquad \left(-f(\nabla\mathbf{u}, \eta, \nabla\eta) + \frac{\partial D^{\mathrm{v}}_{\tau}(\eta)}{\partial \eta} \right) \delta\eta + \delta^+ \overline{D}^{\mathrm{in}}_{\tau}(\eta) \geq 0 \quad \forall \, \delta\eta \in \mathbb{R} \,, \tag{45}$$

where $\delta^+ \overline{D}^{\mathrm{in}}_{\tau}(\eta)$ denotes the *one-sided* derivative of function $\overline{D}^{\mathrm{in}}_{\tau}$ at η in the direction of $\delta\eta \in \mathbb{R}$. Short analysis shows that fulfilment of the conditions (45) jointly is equivalent to (cf. Rockafellar, 1970, Theorem 23.2)

$$f(\nabla\mathbf{u}, \eta, \nabla\eta) - \frac{\partial D^{\mathrm{v}}_{\tau}(\eta)}{\partial \eta} \in \partial \overline{D}^{\mathrm{in}}_{\tau}(\eta) \,. \tag{46}$$

Indeed, if $\eta \in [0, 1]$ so that $\overline{D}^{\mathrm{in}}_{\tau}(\eta)$ is finite then the inequality $(45)_2$ means that the left-hand side term of inclusion (46) is a subgradient of $\overline{D}^{\mathrm{in}}_{\tau}$ at η. Hence, the conditions (45) jointly imply inclusion (46). In turn, if inclusion (46) holds then $\eta \in [0, 1]$ since otherwise $\partial \overline{D}^{\mathrm{in}}_{\tau}(\eta) = \emptyset$, and inequality $(45)_2$ is implied.

With the use of the convex incremental mixed-type dissipation potential

$$\overline{D}_\tau(\eta) = D^{\mathrm{v}}_{\tau}(\eta) + \overline{D}^{\mathrm{in}}_{\tau}(\eta) \,, \tag{47}$$

inclusion (46) takes a more concise form as

$$f(\nabla\mathbf{u}, \eta, \nabla\eta) \in \partial \overline{D}_\tau(\eta) \,. \tag{48}$$

If $\eta \in (0, 1)$, so that the bound constraints for η are inactive in the current time step, then the condition (48) reduces to

$$f(\nabla\mathbf{u}, \eta, \nabla\eta) \in \partial D(\dot{\eta}) \qquad \text{for } \dot{\eta} = \frac{\eta - \eta_n}{\tau} \quad \text{if } \eta \in (0, 1) \,, \tag{49}$$

where $D = D^{\mathrm{v}} + D^{\mathrm{in}}$ as in Section 2.3. In fact, on account of smoothness of D^{v} and positive homogeneity of D^{in}, we respectively have

$$\partial D^{\mathrm{v}}_{\tau}(\eta) = \Big\{ \frac{\partial D^{\mathrm{v}}(\dot\eta)}{\partial \dot\eta}\Big|_{\dot\eta = \frac{\eta-\eta_n}{\tau}} \Big\}\,, \qquad \partial \overline{D}^{\mathrm{in}}(\eta) = \partial D^{\mathrm{in}}(\dot\eta)|_{\dot\eta=\eta-\eta_n} = \partial D^{\mathrm{in}}(\dot\eta)|_{\dot\eta=\frac{\eta-\eta_n}{\tau}} \ \ \forall\, \tau > 0\,. \tag{50}$$

It is concluded that solving the minimization problem (39) with respect to $\eta \in \mathcal{W}_\eta$ for any given $\mathbf{u} \in \mathcal{V}_{\mathbf{u}}$ implies that the constraint $\eta \in [0,1]$ and the inclusion (48) are satisfied a.e. in B. The converse implication is evidently true if potential $\Pi^{\mathrm{v}}_{\tau}[\mathbf{u},\cdot]$ is convex in $\mathcal{W}_\eta$, which in turn is true for τ sufficiently small as proven in Appendix B. The final pointwise condition (49) obtained from the global minimization problem (39) – or leading to it if $\eta \in (0,1)$ in B – is fully consistent with the previously assumed relation (8) for the evolution of η.

Remark 2. In the justification of using the incremental potential for a finite time step, it is essential that the dissipation potential $D(\dot\eta)$ is assumed to be state-independent. In this respect, there is some analogy to a smooth incremental potential for viscoelastic problems, cf. e.g. Lahellec and Suquet (2007); Tůma et al. (2016). However, due to non-smoothness of $D^{\mathrm{in}}(\dot\eta)$ and the presence of bound constraints on η, instead of an equation for the driving force f we have obtained here the inclusion (48) as a consequence of the global minimization (39). The above derivation of the inclusion (48) or (49) does not require convexity of $\Pi^{\mathrm{v}}_{\tau}[\mathbf{u},\cdot]$. If $\Pi^{\mathrm{v}}_{\tau}[\mathbf{u},\cdot]$ is convex, as shown for τ sufficiently small, then $\Pi_{\tau}[\mathbf{u},\cdot]$ is convex and the derivation could be shortened by deducing a global inclusion analogous to (14) directly from the second minimization (39).

2.8. Augmented Lagrangian treatment

The minimization problem (39) is not smooth. To enable an efficient computational treatment, we transform it to a smooth saddle-point problem by using the augmented Lagrangian method that is briefly described below. For a general description of the augmented Lagrangian technique, the reader is referred to Bertsekas (1996), while its application to a non-smooth dissipation potential and bound constraints in a macroscopic model of pseudoelasticity can be found in Stupkiewicz and Petryk (2013). The present treatment follows closely that proposed by Stupkiewicz and Petryk (2013).

Accordingly, the incremental minimization problem (39) is transformed into the following *smooth and unconstrained* saddle-point problem,

$$\text{find} \ \min_{\mathbf{u}\in\mathcal{V}_{\mathbf{u}},\eta\in\mathcal{W}_\eta} \ \max_{\lambda\in\mathcal{W}_\lambda} \ \mathcal{L}[\mathbf{u},\eta,\lambda], \tag{51}$$

for the Lagrange functional $\mathcal{L}$,

$$\mathcal{L}[\mathbf{u},\eta,\lambda] = \Pi^{\mathrm{v}}_{\tau}[\mathbf{u},\eta] + \int_B l(\eta,\lambda)\,\mathrm{d}\mathbf{X}\,, \tag{52}$$

defined as a sum of the regular part Π^{v}_{τ} of the incremental potential Π_τ and the spatial integral of a continuously differentiable function $l(\eta,\lambda)$ which replaces the non-smooth part $\overline{\mathcal{D}}^{\mathrm{in}}_{\tau}$. Here, λ is a scalar field of Lagrange multipliers from a suitable space $\mathcal{W}_\lambda$. Note that the minimization problem with respect to a field of displacements $\mathbf{u}$ remains unchanged, therefore it is not discussed below.

For simplicity we assume below that $f_{\mathrm{c}}^{-} = f_{\mathrm{c}}^{+} = f_{\mathrm{c}}$ so that $D^{\mathrm{in}}(\eta-\eta_n) = f_{\mathrm{c}}|\eta-\eta_n|$. Function $l(\eta,\lambda)$ is then defined as follows (Stupkiewicz and Petryk, 2013):

$$l(\eta,\lambda) = \begin{cases} \lambda(\Delta\eta - \Delta\eta^{-}) + \dfrac{\varrho}{2}(\Delta\eta-\Delta\eta^{-})^2 - f_{\mathrm{c}}\Delta\eta^{-} & \text{if } \hat\lambda \le \varrho\Delta\eta^{-} - f_{\mathrm{c}}, \\ -\dfrac{1}{2\varrho}\left(\lambda^2 + 2f_{\mathrm{c}}\hat\lambda + f_{\mathrm{c}}^2\right) & \text{if } \varrho\Delta\eta^{-} - f_{\mathrm{c}} < \hat\lambda < -f_{\mathrm{c}}, \\ \left(\lambda + \dfrac{\varrho}{2}\Delta\eta\right)\Delta\eta & \text{if } -f_{\mathrm{c}} \le \hat\lambda \le f_{\mathrm{c}}, \\ -\dfrac{1}{2\varrho}\left(\lambda^2 - 2f_{\mathrm{c}}\hat\lambda + f_{\mathrm{c}}^2\right) & \text{if } f_{\mathrm{c}} < \hat\lambda < f_{\mathrm{c}} + \varrho\Delta\eta^{+}, \\ \lambda(\Delta\eta - \Delta\eta^{+}) + \dfrac{\varrho}{2}(\Delta\eta-\Delta\eta^{+})^2 + f_{\mathrm{c}}\Delta\eta^{+} & \text{if } f_{\mathrm{c}} + \varrho\Delta\eta^{+} \le \hat\lambda, \end{cases} \tag{53}$$

where $\Delta\eta = \eta - \eta_n$, $\hat{\lambda} = \lambda + \rho\Delta\eta$ is the augmented Lagrange multiplier, and $\varrho > 0$ is a regularization parameter. The bounds to be enforced on the increment $\Delta\eta$ are denoted by $\Delta\eta^- = -\eta_n$ and $\Delta\eta^+ = 1 - \eta_n$ so that $\Delta\eta^- \leq \Delta\eta \leq \Delta\eta^+$.

Although the above definition of $l(\eta, \lambda)$ may appear complex at a first glance, it has a definite advantage. Namely, a *single* Lagrange multiplier λ is in consequence sufficient to *simultaneously* treat the non-differentiable rate-independent part D^{in} of dissipation and the two inequality constraints on η.

The necessary condition for the saddle point of $\mathcal{L}$, Eq. (51), is the global stationarity condition:

$$\delta\mathcal{L}[\mathbf{u}, \eta, \lambda] = 0 \qquad \forall\, (\delta\mathbf{u}, \delta\eta, \delta\lambda) \in \mathcal{V}^0_{\mathbf{u}} \times \mathcal{W}_\eta \times \mathcal{W}_\lambda, \tag{54}$$

where $\delta\mathcal{L}$ denotes the variation of $\mathcal{L}$ with respect to all its arguments, with $\mathcal{V}^0_{\mathbf{u}} = \{\mathbf{u} \in \mathcal{V}_{\mathbf{u}} \,|\, \mathbf{u} = \mathbf{0} \text{ on } \partial B_u\}$, and is explicitly given by

$$\delta\mathcal{L}[\mathbf{u}, \eta, \lambda] = \int_B \left(\mathbf{S} \cdot \nabla\delta\mathbf{u} + \left(\frac{\partial F}{\partial\eta} + \frac{\partial D^{\text{v}}_\tau}{\partial\eta} + \mu \right) \delta\eta + \frac{\partial F}{\partial\nabla\eta} \cdot \nabla\delta\eta + C\,\delta\lambda \right) \mathrm{d}\mathbf{X} - \int_{\partial B_T} \mathbf{T} \cdot \delta\mathbf{u}\,\mathrm{d}S\,. \tag{55}$$

The last term in Eq. (55) corresponds to the potential $\Omega[\mathbf{u}]$ in the specific form $\Omega[\mathbf{u}] = -\int_{\partial B_T} \mathbf{T} \cdot \mathbf{u}\,\mathrm{d}S$ with $\mathbf{T}$ denoting the nominal traction prescribed on ∂B_T. The contribution resulting from the augmented Lagrangian treatment is expressed in Eqs. (54)–(55) through the 'effective' Lagrange multiplier $\mu(\eta, \lambda)$,

$$\mu(\eta, \lambda) = \frac{\partial l}{\partial\eta} = \begin{cases} \lambda + \varrho(\Delta\eta - \Delta\eta^-) & \text{if } \hat{\lambda} \leq \varrho\Delta\eta^- - f_{\text{c}}, \\ -f_{\text{c}} & \text{if } \varrho\Delta\eta^- - f_{\text{c}} < \hat{\lambda} < -f_{\text{c}}, \\ \lambda + \varrho\Delta\eta & \text{if } -f_{\text{c}} \leq \hat{\lambda} \leq f_{\text{c}}, \\ f_{\text{c}} & \text{if } f_{\text{c}} < \hat{\lambda} < f_{\text{c}} + \varrho\Delta\eta^+, \\ \lambda + \varrho(\Delta\eta - \Delta\eta^+) & \text{if } f_{\text{c}} + \varrho\Delta\eta^+ \leq \hat{\lambda}, \end{cases} \tag{56}$$

and through function $C(\eta, \lambda)$ that describes a state-dependent constraint, as explained below,

$$C(\eta, \lambda) = \frac{\partial l}{\partial\lambda} = \begin{cases} \Delta\eta - \Delta\eta^- & \text{if } \hat{\lambda} \leq \varrho\Delta\eta^- - f_{\text{c}}, \\ -\dfrac{1}{\varrho}(\lambda + f_{\text{c}}) & \text{if } \varrho\Delta\eta^- - f_{\text{c}} < \hat{\lambda} < -f_{\text{c}}, \\ \Delta\eta & \text{if } -f_{\text{c}} \leq \hat{\lambda} \leq f_{\text{c}}, \\ -\dfrac{1}{\varrho}(\lambda - f_{\text{c}}) & \text{if } f_{\text{c}} < \hat{\lambda} < f_{\text{c}} + \varrho\Delta\eta^+, \\ \Delta\eta - \Delta\eta^+ & \text{if } f_{\text{c}} + \varrho\Delta\eta^+ \leq \hat{\lambda}. \end{cases} \tag{57}$$

Since $l(\eta, \lambda)$ is continuously differentiable, both μ and C are continuous functions of η and λ.

Let us examine in more detail how the augmented Lagrangian method works in the present context. As before, the two terms that involve the variation of the displacement $\delta\mathbf{u}$ in the stationarity condition (54)–(55) are recognized as the equilibrium equation in weak form.

In turn, the vanishing variation of $\mathcal{L}$ with respect to λ implies that $C(\eta, \lambda) = 0$ must hold at the solution. Accordingly, the pointwise stationarity condition $C(\eta, \lambda) = 0$ specifies the constraint that is enforced either on η or on λ, depending on the actual state defined by the augmented Lagrange multiplier $\hat{\lambda}$. The state is defined for the whole (η, λ)-space: the five zones I–V indicated in Fig. 2b are separated by the (broken) lines of constant $\hat{\lambda}$ and correspond to the respective branches (enumerated from top to bottom) in Eqs. (53), (56) and (57). Specifically, zones II and IV correspond to an active transformation with $\Delta\eta < 0$ and $\Delta\eta > 0$, respectively. The respective branches of the constraint $C(\eta, \lambda) = 0$ imply then $\lambda = -f_{\text{c}}$ or $\lambda = f_{\text{c}}$, the values actually assumed by μ in the respective zones, see Eq. (56). Zone III corresponds to a stalled transformation with the constraint $\Delta\eta = 0$ enforced directly on η. Finally, the bound constraint $\Delta\eta = \Delta\eta^-$ is active in zone I, and similarly $\Delta\eta = \Delta\eta^+$ in zone V. Note that, for $\eta_n = 0$ or $\eta_n = 1$, zones I–III or III–V, respectively, collapse to a single zone in which the constraint $C(\eta, \lambda) = 0$ implies $\Delta\eta = 0$.

On substituting the above consequences of $C(\eta, \lambda) = 0$ into the equations (56), it follows that the effective Lagrange multiplier μ that appears in the stationarity condition (54)–(55) is just equal to the actual

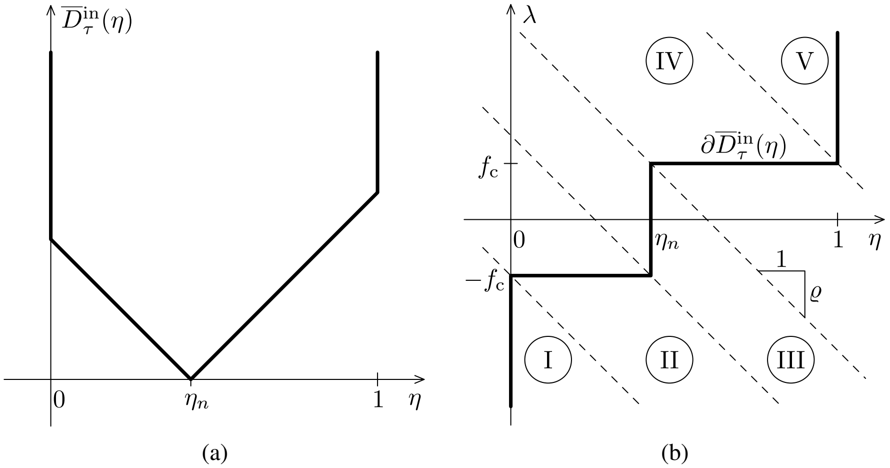

(a) (b)

Figure 2: Non-smooth part $\overline{D}^{\mathrm{in}}_\tau(\eta) = D^{\mathrm{in}}(\eta-\eta_n) + I_{[0,1]}(\eta)$ of the integrand of the incremental potential Π_τ and the graph of admissible values of (η,λ).

Lagrange multiplier λ. It is easy to check that the converse implication is also true, hence

$$\mu = \lambda \quad \Longleftrightarrow \quad C(\eta,\lambda) = 0\,. \tag{58}$$

Furthermore, it can be directly verified that another important consequence holds true, viz.

$$\lambda \in \partial\overline{D}^{\mathrm{in}}_\tau(\eta) \qquad \text{if } C(\eta,\lambda) = 0\,. \tag{59}$$

The graph of values of the pairs (η,λ) admitted by the stationarity condition $C(\eta,\lambda) = 0$ has the form indicated in Fig. 2b.

Remarkably, a solution (η,λ) to the smooth stationarity problem $\delta_\lambda\mathcal{L} = 0$ turns out to satisfy exactly the inclusion (59) that characterizes a non-smooth problem. Therefore, λ has the interpretation as the subgradient of the non-smooth part $\overline{D}^{\mathrm{in}}_\tau$ of the integrand of the incremental potential Π_τ, cf. Fig. 2a and Eq. (38). These important conclusions hold true irrespectively of the adopted positive value of parameter ϱ, which is a distinctive feature of the augmented Lagrangian method, in contrast to the penalty function method.

When $\delta_\lambda\mathcal{L} = 0$, stationarity of $\mathcal{L}$ with respect to η is expressed, on using Eqs. (55), (42) and (58), as follows

$$\delta_\eta\mathcal{L}[\mathbf{u},\eta,\lambda] = \int_B \left(-f(\nabla\mathbf{u},\eta,\nabla\eta) + \frac{\partial D^{\mathrm{v}}_\tau(\eta)}{\partial\eta} + \lambda \right) \delta\eta \,\mathrm{d}\mathbf{X} = 0 \qquad \forall\, \delta\eta \in \mathcal{W}_\eta\,. \tag{60}$$

Hence, $\delta_\lambda\mathcal{L} = 0$ and $\delta_\eta\mathcal{L} = 0$ jointly imply that the following pointwise condition

$$f(\nabla\mathbf{u},\eta,\nabla\eta) - \frac{\partial D^{\mathrm{v}}_\tau(\eta)}{\partial\eta} = \lambda \tag{61}$$

is satisfied a.e. in B. With the above interpretation of λ as a subgradient of $\overline{D}^{\mathrm{in}}_\tau(\eta)$, the condition (61) is equivalent to

$$f(\nabla\mathbf{u},\eta,\nabla\eta) - \frac{\partial D^{\mathrm{v}}_\tau(\eta)}{\partial\eta} \in \partial\overline{D}^{\mathrm{in}}_\tau(\eta)\,. \tag{62}$$

This coincides with the pointwise condition (46) obtained earlier on another route as the condition necessary for a minimum (39) of $\Pi_\tau[\mathbf{u},\eta]$. When $\Pi_\tau[\mathbf{u},\cdot]$ is convex (which is the case when τ is sufficiently small) then solving the stationarity problem (54) for the augmented Lagrangian with respect to (λ,η)-fields is equivalent to minimization of $\Pi_\tau[\mathbf{u},\eta]$ in $\mathcal{W}_\eta$.

Remark 3. The justification of reducing the minimization problem (39) with respect to η-field to the stationarity problem (54) with respect to (η,λ)-fields has been completed. It is remarkable that the key inclusion (46) associated with the original *non-smooth* minimization problem (39) is implied just by *stationarity* of the augmented Lagrangian (52) with respect to (η,λ)-fields. The facts that $\mathcal{L}[\mathbf{u},\eta,\lambda]$ is concave with respect to λ and convex with respect to η for τ small enough have not been used in the above derivation of inclusion (62). It is worth noting that convexity of $\Pi_\tau^{\rm v}[\mathbf{u},\cdot]$ (for τ small enough) is preserved by the addition of the integrand function $l(\eta,\lambda)$ that is concave with respect to λ and convex with respect to η by construction.

Remark 4. For completeness, we provide here the set of governing equations in the strong (local) form. They are straightforwardly obtained as the Euler–Lagrange equations for the stationarity problem (54) and read

$$\operatorname{Div}\mathbf{S}(\nabla\mathbf{u},\eta)=\mathbf{0},\qquad \frac{\eta-\eta_n}{\tau L}=f(\nabla\mathbf{u},\eta,\nabla\eta)-\mu(\eta,\lambda),\qquad C(\eta,\lambda)=0. \tag{63}$$

The first equation is the standard equilibrium equation that results from stationarity of $\mathcal{L}$ with respect to the displacement field $\mathbf{u}$. The second equation results from stationarity of $\mathcal{L}$ with respect to the order parameter η and represents a time-discrete evolution equation for η. The thermodynamic driving force f is here amended by the effective Lagrange multiplier μ, Eq. (56), which handles the rate-independent threshold on the driving force as well as the bound constraints. The third equation, discussed in detail above, is a pointwise state-dependent constraint that results from stationarity of $\mathcal{L}$ with respect to the Lagrange multiplier λ.

3. Finite element implementation

The finite element method is used in this work for the spatial discretization of the governing equations. Note that the spectral methods, which are most often used in the context of the phase-field method (e.g., Wang and Khachaturyan, 1997; Artemev et al., 2000; Ahluvalia et al., 2004), lead to highly efficient computational schemes, particularly, when combined with the semi-implicit time integration scheme (Chen and Shen, 1998). However, this comes at the cost of severe restrictions concerning the shape of the domain and the requirement of periodic boundary conditions. The finite element method is much more flexible in this respect, see, for instance, the micro-pillar example of Section 4.3 which combines a non-cuboidal domain and unilateral contact interactions. Furthermore, finite deformations and the related nonlinearities can be directly treated by the finite element method (e.g., Levitas et al., 2009; Clayton and Knap, 2011; Hildebrand and Miehe, 2012).

The finite-element implementation is developed starting from the stationarity condition (54) for the augmented Lagrangian $\mathcal{L}$. Recall that condition (54) describes a time-discrete problem that results from application of the backward-Euler time integration scheme, cf. Section 2.7.

The present finite-element treatment follows closely that employed in our earlier work (Tůma et al., 2016; Tůma and Stupkiewicz, 2016). Four-node quadrilateral elements (eight-node hexahedral elements in 3D) are used so that a piecewise bilinear approximation (trilinear approximation in 3D) is obtained for all unknown fields: displacement $\mathbf{u}$, order parameter η and Lagrange multiplier λ. Numerical integration is performed using the standard Gaussian quadrature, except for the constraint C, i.e., the term that is weighted by the test function $\delta\lambda$ in Eq. (55), which is integrated using the nodal quadrature so that the non-smooth complementarity conditions, which are enforced by C on η and λ, are adequately treated. The global system of nonlinear equations that result from the finite-element discretization is solved simultaneously with respect to all unknowns using a (semi-smooth) Newton method.

To avoid mutually inconsistent approximation of $\mathbf{F}$ and $\mathbf{F}_{\rm t}$, the latter, which depends on η through Eq. (25), is evaluated at the element center, and its element-wise constant approximation is used, see Tůma et al. (2016) for more details. The matrix exponential that is involved in the logarithmic mixing rule (25) is efficiently implemented, along with its first and second derivative, using the closed-form representation developed by Korelc and Stupkiewicz (2014), see also Hudobivnik and Korelc (2016).

The augmented Lagrangian technique, which is used to implement the rate-independent dissipation and the bound constraints on η, is an extension of that used previously to enforce the bound constraints alone (Tůma et al., 2016; Tůma and Stupkiewicz, 2016). While the details, notably the form of the augmented

Lagrangian function $l(\eta, \lambda)$, clearly differ, the computational treatment is, in principle, the same, except that irregularities occur here not only at $\eta = 0$ and $\eta = 1$ but also at $\eta = \eta_n$. It is worth emphasizing that thanks to the augmented Lagrangian method used, the incorporation of the rate-independent dissipation into the phase-field modelling approach has turned out not so computationally demanding as it might be expected beforehand. Following Tůma and Stupkiewicz (2016), the basic formulation of the augmented Lagrangian method outlined in Section 2.8 has been improved by introducing a single variable that represents, at each node, either the order parameter η or the corresponding Lagrange multiplier λ. This treatment amounts to directly enforcing the point (η, λ) to lie on the solid line in Fig 2b, so that one variable can be eliminated. The total number of unknowns is thus significantly reduced. As the convergence behaviour is not noticeably affected, the total CPU time is also reduced, even though the symmetry of the tangent matrix is lost. The present improved formulation is similar to that developed, in a different context of cavitation in hydrodynamic lubrication, by Lengiewicz et al. (2014, Appendix C), where more details can be found.

The model has been implemented in the *AceGen/AceFEM* system (Korelc, 2002, 2009). *AceGen* is a code generation system that employs an automatic differentiation (AD) technique, while *AceFEM* is a flexible finite-element environment that is closely integrated with *AceGen*. As a result, an efficient and robust implementation of the model has been achieved. An exact tangent matrix has been derived using the AD technique implemented in *AceGen*, which is crucial for achieving the quadratic convergence rate of the Newton method. A direct linear solver (Intel MKL PARDISO) has been used in the computations.

4. Examples

4.1. Coarsening and arrest of microstructure in an unconstrained domain

The first example illustrates the fundamental qualitative difference between microstructure evolution governed by the purely viscous dissipation ($\mathcal{D} = \mathcal{D}^{\mathrm{v}}$) and by the mixed-type dissipation that combines the viscous and rate-independent terms ($\mathcal{D} = \mathcal{D}^{\mathrm{v}} + \mathcal{D}^{\mathrm{in}}$).

Consider transition between two phases, identified here with two variants of martensite, within a two-dimensional domain B that occupies in the reference configuration a square of side length a. The two variants are characterized by transformation stretches $\mathbf{U}_1$ and $\mathbf{U}_2$ that correspond to $\eta = 0$ and $\eta = 1$, respectively,

$$\mathbf{U}_1 = \begin{pmatrix} \gamma & 0 \\ 0 & \alpha \end{pmatrix}, \qquad \mathbf{U}_2 = \begin{pmatrix} \alpha & 0 \\ 0 & \gamma \end{pmatrix}, \tag{64}$$

where α and γ are stretch parameters. The reference configuration is identified with that of an unstressed parent phase with $\mathbf{F}_{\mathrm{t}} = \mathbf{I}$, however, the parent phase itself is not considered here.

A random distribution of the order parameter η, which is varied between 0.4 and 0.6 in B, is adopted as the initial condition, and evolution of the system from this initial state is simulated until a steady state is attained. The boundary ∂B is free, i.e. zero traction and no displacement boundary condition are applied to ∂B, except that the rigid-body motion is constrained, and the boundary condition (29) is assumed for η.

Material parameters are adopted such that the problem corresponds to martensite variant rearrangement in a CuAlNi shape memory alloy. Specifically, a compound twinning system is considered along with the corresponding two variants of the orthorhombic γ_1' (2H) martensite. The orientation of the crystal is adopted such that the two twinning planes predicted by the crystallographic theory are oriented at $\pm 45^\circ$ (in the reference configuration). Accordingly, $\mathbf{U}_1$ and $\mathbf{U}_2$ in Eq. (64) represent the respective rotated transformation stretch tensors in two dimensions with $\alpha = 1.0619$ and $\gamma = 1.0230$ (Bhattacharya, 2003).

Elastic constants of the orthorhombic γ_1' martensite in CuAlNi are taken from the literature (Yasunaga et al., 1983). The bulk free energy in a stress-free state is identical for the two variants, hence we put $F_1^0 = F_2^0 = 0$. The energy of twin boundaries is assumed as $\gamma = \gamma_{\mathrm{tw}} = 0.02$ J/m^2, similarly as in our previous studies (Petryk et al., 2010; Tůma et al., 2016), and the interface thickness parameter is adopted as $\ell = 2.5\,\mathrm{nm}$. Three values of the critical driving force f_{c} are used in the simulations, namely $f_{\mathrm{c}} = 0.5, 1$ and $2\,\mathrm{MPa}$, in addition to $f_{\mathrm{c}} = 0$ in the case of purely viscous dissipation. Finally, the mobility parameter is set equal to $L = 0.1$ (Pa s)$^{-1}$. Note, however, that L defines here the time scale and otherwise does not influence the results. The material parameters are summarized in Table 1 (note that only four out of nine elastic constants are needed in the two-dimensional problem of compound twinning).

Table 1: Material parameters: compound twinning in CuAlNi.

Transformation stretch		Elastic constants				Phase-field constants			
α	γ	c_{11}	c_{33}	c_{55}	c_{13}	$\gamma_{\rm tw}$	ℓ	L	$f_{\rm c}$
1.0619	1.0230	189 GPa	205 GPa	19.7 GPa	45.5 GPa	0.02 J/m^2	2.5 nm	0.1 (Pa s)$^{-1}$	0–2 MPa

A regular mesh of quadrilateral elements has been used with the element size $h = 2.2\,$nm adopted such that the diffuse interfaces can be resolved to sufficient detail (recall that the thickness of an unstressed interface is $\pi\ell$). For the two domain sizes studied in this section, the computational domain is discretized into 682×682 elements for $a = 1.5\,\mu$m and into 1364×1364 elements for $a = 3\,\mu$m, with over five million degrees of freedom in the latter case.

Figure 3 shows selected snapshots of microstructure evolution simulated for $f_{\rm c} = 0$ and $f_{\rm c} = 1\,$MPa within the smaller domain, $a = 1.5\,\mu$m, both starting from the same initial distribution of the order parameter. A movie showing the complete evolution is provided as a supplementary material accompanying this paper.

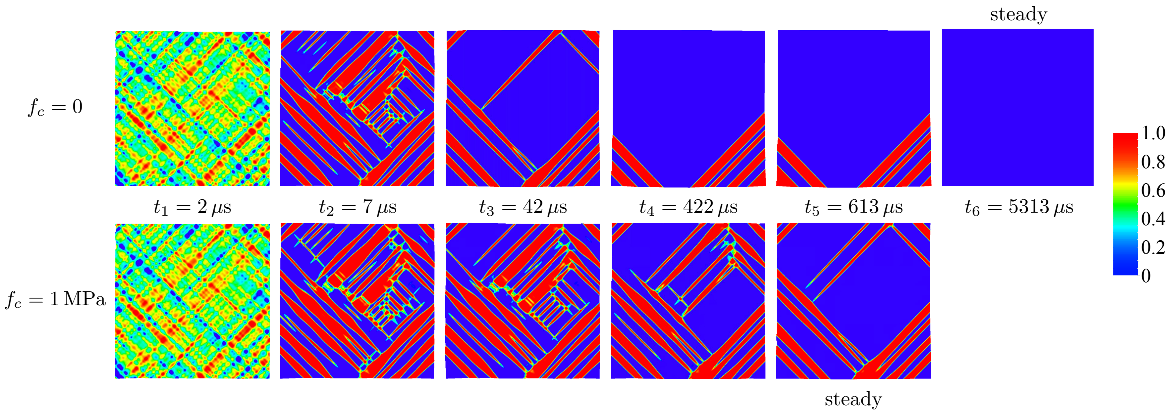

Figure 3: Microstructure evolution in the domain of the size $a = 1.5\,\mu$m for the viscous dissipation ($f_{\rm c} = 0$, top row) and for the mixed-type dissipation with $f_{\rm c} = 1\,$MPa (bottom row). The color map indicates the order parameter with $\eta = 0$ (blue) and $\eta = 1$ (red) corresponding to the martensite variant 1 and 2, respectively.

Since there is no external loading, the system evolves such that the total free energy is decreasing. Specifically, the evolution is driven by the interfacial energy and by local stresses, which are induced by local incompatibilities in the microstructure. As a result, coarsening of the microstructure is observed in both cases. However, there is a fundamental qualitative difference between the two models. For a purely viscous dissipation ($f_{\rm c} = 0$), the final state, which is achieved after a sufficiently long time, is a pure single variant, for which the total free energy attains a global minimum (with the elastic strain energy and the interfacial energy equal to zero).

The situation is very different when rate-independent dissipation is included in the model with a nonzero threshold driving force (here $f_{\rm c} = 1\,$MPa). Accordingly, microstructure evolution stops when the driving forces no longer exceed the threshold value imposed by the rate-independent part of dissipation. Hence a non-trivial final (steady-state) microstructure is achieved, as illustrated in Fig. 3.

Figure 4 shows the evolution of the total free energy $\mathcal{F} = \mathcal{F}_{\rm B} + \mathcal{F}_\Gamma$ along with its bulk $\mathcal{F}_{\rm B}$ and interfacial $\mathcal{F}_\Gamma$ contributions that are obtained by integrating the respective densities $F_{\rm B}$ and F_Γ. The total energy monotonically decreases in time, as implied by the minimization principle (33) when $\Omega = 0$. Evolution of the individual contributions is more complex. The initial condition of random η close to 0.5 corresponds to a high interfacial energy $\mathcal{F}_\Gamma$ while the elastic strain energy $\mathcal{F}_{\rm B}$ is relatively low. In the first stage, a fine microstructure forms, see the snapshots corresponding to $t = t_2$, and this is associated with a decrease of the interfacial energy at the expense of a significant increase of the elastic strain energy. Subsequently, both energy contributions decrease monotonically. For the viscous dissipation ($f_{\rm c} = 0$), during the last stage of evolution, e.g., at $t = t_4$ and $t = t_5$, the microstructure consists of parallel planar interfaces located in the corners of the domain. The elastic strain energy is then much smaller than the interfacial energy, and the evolution is driven solely by the interfacial energy, which decreases as the interfaces move towards the vertices. As can be seen in Fig. 3, for mixed-type dissipation ($f_\mathrm{c} = 1\,\mathrm{MPa}$), similar isolated planar interfaces located in the corners are stationary. This means that the corresponding driving forces are insufficient to overcome the threshold f_c. The related effects are studied analytically in Section 4.2.

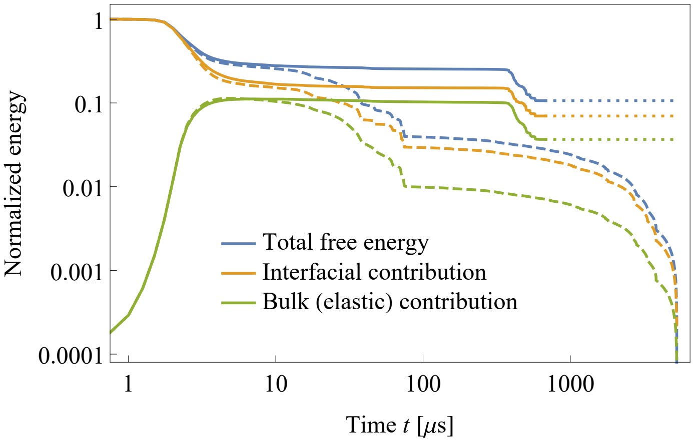

Figure 4: Evolution of the total free energy $\mathcal{F}$ and its interfacial and bulk (elastic strain) contributions for the viscous dissipation ($f_\mathrm{c} = 0$, dashed lines) and for the mixed-type dissipation ($f_\mathrm{c} = 1\,\mathrm{MPa}$, solid lines, the final steady-state stage is marked by dotted lines). The energies are normalized by the initial total free energy, and a log–log scale is used to reveal more details of the evolution.

The effect of the threshold driving force f_c on the final microstructure is illustrated in Fig. 5 for the larger domain ($a = 3\,\mu\mathrm{m}$). Specifically, three values of f_c are considered, $f_\mathrm{c} = 0.5, 1, 2\,\mathrm{MPa}$. Furthermore, the evolution starting from three random initial conditions is simulated for each f_c. The case of the viscous dissipation ($f_\mathrm{c} = 0$) has not been simulated because the final result is essentially known (uniform single variant), and the corresponding computational cost would be very high in view of the long physical time needed for all the interfaces to vanish (see Section 4.2). The high computational cost has actually been the reason why the simulations reported in Fig. 3 have been carried out for a smaller domain.

It can be seen in Fig. 5 that the final microstructure gets coarser as f_c decreases. This general feature is observed for the three initial conditions studied, the details of the microstructure being, of course, dependent on the initial condition. It is worth noting that the microstructures obtained for higher values of f_c resemble qualitatively the experimental microstructures reported by Chu (1993).

4.2. Interface migration driven by the interfacial energy

As illustrated in the previous subsection, the microstructure freezes due to the rate-independent part of dissipation. In this subsection, we investigate this effect further by considering a single interface located at the corner of an unconstrained domain and by studying its migration driven solely by the interfacial energy. A simple analytical sharp-interface model is first developed for that purpose, and its predictions are next compared to results of phase-field simulations.

Consider a planar *sharp* interface (twinning plane) separating two phases (martensite variants) that occupy a quadrant, see Fig. 6. The phases are assumed compatible, hence the kinematic compatibility condition at the interface is satisfied at zero stress, and mechanical equilibrium is thus trivially satisfied. The interface is oriented at 45 degrees, and its position along the ξ-axis that is perpendicular to the interface is specified by $\xi = \varsigma$ with $\xi = 0$ corresponding to the vertex. The length of the interface is thus $w = 2\varsigma$.

Considering that the elastic strain energy is equal to zero, the interfacial energy is the only contribution to the total free energy $\hat{\mathcal{F}}$. Denoting by γ the interfacial energy density, we have thus

$$\hat{\mathcal{F}} = w\gamma = 2\varsigma\gamma, \tag{65}$$

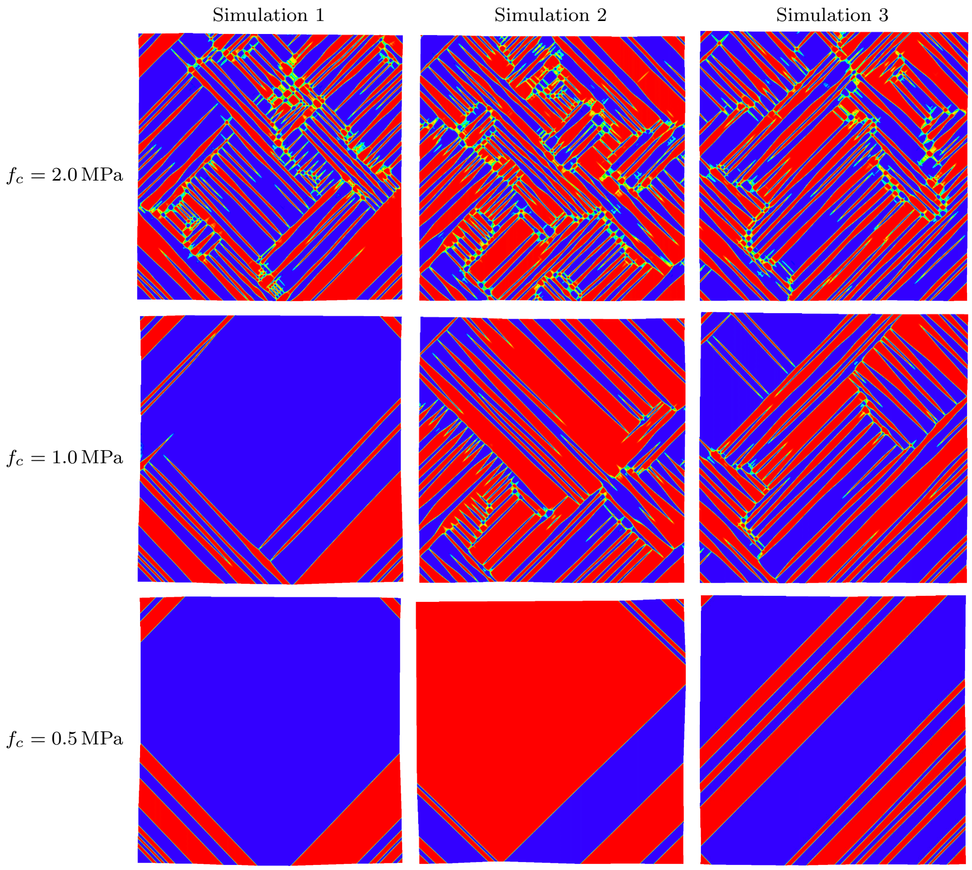

Figure 5: Steady-state microstructures in the domain of the size $a = 3\,\mu$m obtained for the mixed-type dissipation with different values of the critical driving force f_c and for three initial random distributions of the order parameter η.

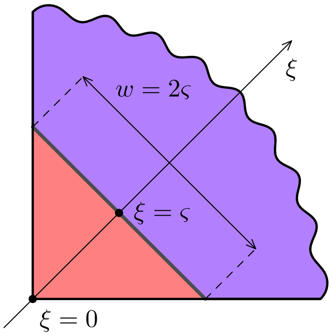

Figure 6: Interface migration driven by the interfacial energy: sketch of the problem.

where $\hat{\mathcal{F}}$ is the energy per unit thickness in the normal direction, and the chemical energy is assumed equal to zero, $F_1^0 = F_2^0 = 0$, as in the previous subsection. It is obvious that propagation of the interface towards the vertex would lower the free energy, hence a nonzero driving force for such an evolution exists.

Propagation of the interface is associated with dissipation of energy. In analogy to the phase-field model of Section 2, the local dissipation potential $\hat{D}$ is assumed to comprise a viscous contribution and a rate-independent one,

$$\hat{D} = \frac{1}{2\hat{L}}\, v_n^2 + \hat{f}_{\mathrm{c}}|v_n|, \qquad v_n = \dot{\varsigma}, \tag{66}$$

where v_n is the propagation speed (in the normal direction), $\hat{L} > 0$ is the effective mobility of the interface and $\hat{f}_{\mathrm{c}} \geq 0$ is the effective critical driving force. The global dissipation potential is thus

$$\hat{\mathcal{D}} = w\hat{D} = 2\varsigma \left(\frac{1}{2\hat{L}}\, \dot{\varsigma}^2 + \hat{f}_{\mathrm{c}}|\dot{\varsigma}| \right), \tag{67}$$

and the global rate potential $\hat{\Pi}$ is defined as

$$\hat{\Pi} = \frac{\mathrm{d}\hat{\mathcal{F}}}{\mathrm{d}t} + \hat{\mathcal{D}}. \tag{68}$$

Evolution of the system can now be determined by minimizing $\hat{\Pi}$ which is a convex function of $\dot{\varsigma}$. The solution is straightforwardly obtained in the form

$$\dot{\varsigma} = \begin{cases} \dfrac{\hat{L}(\varsigma \hat{f}_{\mathrm{c}} - \gamma)}{\varsigma} < 0 & \text{if } \ \varsigma < \varsigma_{\mathrm{c}}, \\ 0 & \text{if } \ \varsigma \geq \varsigma_{\mathrm{c}}, \end{cases} \qquad \text{where } \ \varsigma_{\mathrm{c}} = \frac{\gamma}{\hat{f}_{\mathrm{c}}}. \tag{69}$$

It follows that propagation of the interface is blocked by the rate-independent dissipation if the length of the interface is greater than or equal to the critical length $w_{\mathrm{c}} = 2\varsigma_{\mathrm{c}}$, i.e. if $w \geq w_{\mathrm{c}}$. Otherwise, if $w < w_{\mathrm{c}}$, the interface propagates towards the vertex with a speed that depends on the position of the interface. Ultimately, the interface reaches the vertex and disappears. For the viscous dissipation, i.e. for $\hat{f}_{\mathrm{c}} = 0$, the interface propagates with a nonzero speed regardless of its position,

$$\dot{\varsigma} = -\frac{\hat{L}\gamma}{\varsigma} \qquad \text{for } \ \hat{f}_{\mathrm{c}} = 0, \tag{70}$$

and the interface disappears once it reaches the vertex.

Qualitatively, the solution derived above fully agrees with the behavior observed in the phase-field simulations reported in the previous subsection. In order to perform a quantitative comparison, the effective mobility $\hat{L}$ and the effective critical driving force $\hat{f}_{\mathrm{c}}$ must be determined in terms of the respective parameters of the phase-field model. This is accomplished below by considering a propagating diffuse interface and by integrating the corresponding local dissipation potential. For the double-obstacle potential (23), the profile of the diffuse interface with its center located at $\xi = \varsigma(t)$ is given by Eq. (A.5) in Appendix A, and its time derivative is nonzero within the diffuse interface, $\dot{\eta} = -\frac{\dot{\varsigma}}{2\ell}\cos\left(\frac{\xi-\varsigma}{\ell}\right)$, and zero elsewhere. The effective dissipation potential for a sharp interface is obtained by integrating the local dissipation potential D, namely

$$\hat{D} = \int_{-\infty}^{+\infty} D \,\mathrm{d}\xi = \int_{\varsigma-\pi\ell/2}^{\varsigma+\pi\ell/2} \left(\frac{1}{2L}\dot{\eta}^2 + f_\mathrm{c}|\dot{\eta}|\right)\mathrm{d}\xi = \frac{\pi\dot{\varsigma}^2}{16\ell L} + f_\mathrm{c}|\dot{\varsigma}|. \tag{71}$$

Comparing the above result to the definition of $\hat{D}$ in Eq. (66), the effective mobility and critical driving force are identified as

$$\hat{L} = \frac{8\ell L}{\pi}, \qquad \hat{f}_\mathrm{c} = f_\mathrm{c}. \tag{72}$$

The excellent agreement between the analytical solution (69) and the results of phase-field computations is illustrated in Fig. 7. In particular, both the propagation speed $v = \dot{\varsigma}$ and the critical length $w_\mathrm{c} = 2\varsigma_\mathrm{c}$ are correctly represented by the phase-field model. The results reported in Fig. 7 correspond to the parameters used in the previous subsection. In the phase-field simulations, the propagation speed has been obtained in terms of the position of the isoline of $\eta = 0.5$ along the ξ-axis at two consecutive time steps.

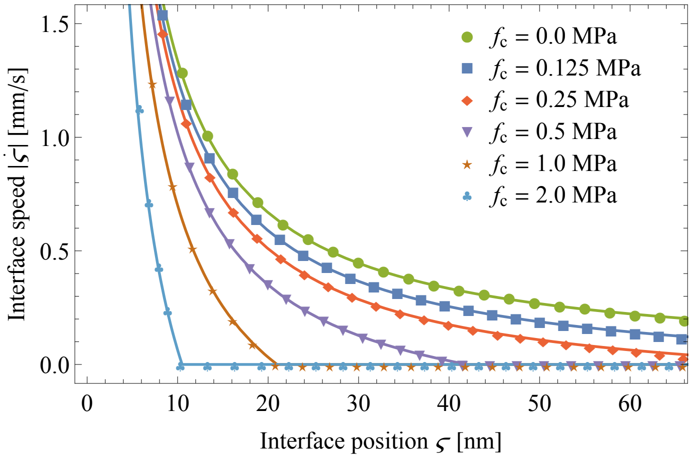

Figure 7: Dependence of the interface speed $\dot{\varsigma}$ on its position ς for different values of threshold parameter f_c. The analytical estimate (solid lines) is compared to the phase-field results (markers).

In the analytical sharp-interface model derived above, the interface is perfectly planar, and its propagation is driven by the interfacial energy alone, the elastic strains and the related stresses being equal to zero. The respective diffuse interfaces visible in Figs. 3 and 5 seem to be planar, but in fact they are not exactly planar. This is clear once one notices that the natural boundary condition (29) is enforced on the order parameter η. The diffuse interface is thus orthogonal to both boundaries, and it is curved in the vicinity of the boundaries so that it can take the theoretical orientation in the interior of the domain. The local incompatibility at the boundaries generates elastic strains and stresses that provide the actual driving force for the propagation of the diffuse interface.

To illustrate the mechanism discussed above, additional simulations have been performed in which artificial material parameters have been used such that the curvature of the interface is more pronounced. Specifically, $\mathbf{F}_\mathrm{t}$ and $\mathbf{L}$ have been redefined according to

$$\mathbf{F}_\mathrm{t}^\theta = \exp(\log \mathbf{U}_1 + \theta\eta(\log \mathbf{U}_2 - \log \mathbf{U}_1)), \qquad \mathbf{L}^\theta = \mathbf{L}_1 + \theta\eta(\mathbf{L}_2 - \mathbf{L}_1), \tag{73}$$

where $0 \le \theta \le 1$ is a scaling parameter. Accordingly, for $\theta = 0$, the transformation does not result in any change in $\mathbf{F}_\mathrm{t}^\theta = \mathbf{U}_1$ and $\mathbf{L}^\theta = \mathbf{L}_1$, while the original model is recovered for $\theta = 1$. Characteristic shapes of the interfaces that propagate in a quasi-steady-state manner are shown in Fig. 8 for selected values of θ. As θ is decreased, the curved parts of the interface in the vicinity of the boundaries are more pronounced.

Ultimately, for $\theta = 0$, the phase-field equation is fully decoupled from the equilibrium equation (which is trivially satisfied by $\nabla \mathbf{u} = \text{const}$), and the interface is a circular arc.

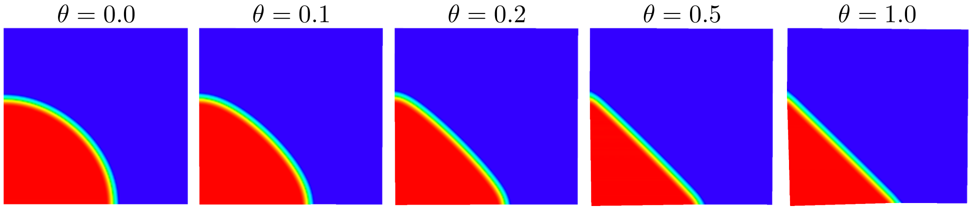

Figure 8: Interface shape depends on the elastic strain energy needed to maintain compatibility of a non-planar interface (relative to the interfacial energy). Domain size is here $a = 100$ nm.

4.3. *Compression of a micro-pillar*

In the last example, we want to mimic the experiment by San Juan et al. (2009) in which a [001]-oriented CuAlNi micro-pillar was compressed using an instrumented nano-indentation device with a sphero-conical diamond indenter tip. The geometry is shown in Fig. 9a, and the 3D mesh in Fig. 9b. As in the experiment, the height of the micro-pillar and its diameter at the bottom and the top are, respectively, $h = 3.8\,\mu$m, $2R_1 = 0.9\,\mu$m and $2R_2 = 0.75\,\mu$m. The pillar is compressed by a rigid sphere of the radius $R_\text{b} = 0.6\,\mu$m, and frictionless contact has been assumed in the computations. In order to ensure realistic boundary conditions at the bottom support, a part of the substrate is included in the model, and the displacements are constrained on its outer boundary, as indicated in Fig. 9a.

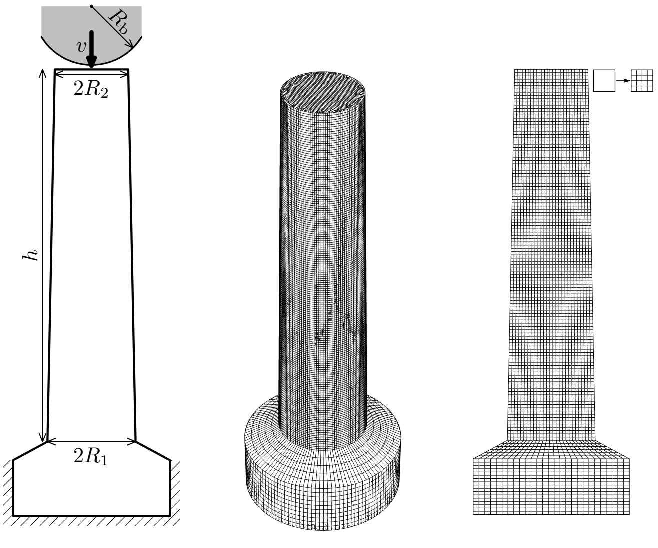

(a) (b) (c)

Figure 9: Compression of the micro-pillar: (a) dimensions, (b) 3D mesh, (c) 2D mesh (the 2D mesh shown in the figure is four times coarser than that used in the computations).

The experimental pseudoelastic response of the micro-pillar (San Juan et al., 2009) is shown in Fig. 10 (marked by red dots). The maximum displacement of about 140 nm corresponds to the average compressive strain of about 3.7%, of which the inelastic strain is about 3%. This value is more than twice smaller (see below) than the transformation strain corresponding to uniaxial compression of the [001]-oriented CuAlNi alloy transforming to the monoclinic β_1' martensite that, according to San Juan et al. (2009), would be stress-induced in the test conditions. There can be several reasons for this discrepancy, for instance, incomplete transformation of the pillar or formation of a microstructure composed of several martensite variants including those that are not oriented favorably with respect to the load. Another option is that the orthorhombic γ_1' martensite might actually be stress-induced in this nano-compression test, even though the cubic-to-monoclinic transformation was observed in the macroscopic compression tests on single crystals of the same alloy (San Juan et al., 2009). Note that the transformation strain of the habit-plane variant (HPV) of the (twinned) orthorhombic γ_1' martensite is about 4.4%, which is much closer to the experimentally observed strain of 3%, and this phase transition is usually characterized by a large hysteresis due to the twinning mechanism involved in the formation of the austenite–martensite interface (Zhang et al., 2009).

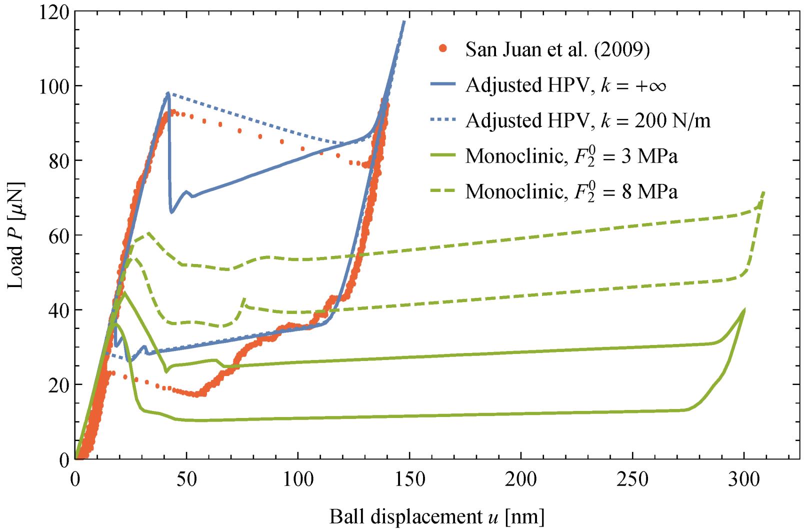

Figure 10: Compression of the micro-pillar: load–depth response predicted by the phase-field model for four sets of model parameters (see text) and the experimental data of San Juan et al. (2009).

Due to the complexities mentioned above, a fully predictive simulation of the nano-compression test of San Juan et al. (2009) is not attempted in this work. Rather, this numerical example is intended to further illustrate the consequences of including the rate-independent dissipation into the phase-field framework and the capabilities of the present computational scheme. Accordingly, in the following, the martensite is assumed to be characterized by the following transformation stretch (Bain strain),

$$\mathbf{U}_2 = \begin{pmatrix} 1/\lambda & 0 & 0 \\ 0 & 1 & 0 \\ 0 & 0 & \lambda \end{pmatrix}, \tag{74}$$

where the stretch parameter $\lambda = 0.97$ corresponds to the compressive transformation strain of 3%, and yields a very good approximation of the experimental pseudoelastic response, cf. the solid and dotted blue lines in Fig. 10. The dotted blue line in Fig. 10 shows the effect of compliance of the loading device (with the corresponding stiffness $k = 200\,\text{N/m}$) as discussed in more detail at the end of this subsection.

The components of $\mathbf{U}_2$ in Eq. (74) are given in a coordinate system with its x_3-axis aligned with the axis of the pillar. The configuration of the unstressed austenite is adopted as the reference configuration, thus $\mathbf{U}_1 = \mathbf{I}$. Further, the chemical energies $F_1^0 = 0$ and $F_2^0 = 3\,\text{MPa}$ and the critical driving force $f_\text{c} = 1.2\,\text{MPa}$ have been adopted such that the hysteresis loop approximates well the experimental one. The elastic constants of the cubic austenite (Suezawa and Sumino, 1976) are adopted for both the austenite and the martensite. For the energy of austenite–martensite interfaces, the value of $\gamma = 0.2\,\text{J/m}^2$, as in (Tůma et al., 2016), has been assumed in the computations. The interface thickness parameter has been set as $\ell = 30\,\text{nm}$ (the average element size is $20\,\text{nm}$), and the mobility parameter has been set equal to $L = 0.1\,(\text{Pa}\,\text{s})^{-1}$. Loading is here applied by prescribing a constant velocity v of the rigid ball with $v = 0.025\,\text{mm/s}$ or $v = 0.175\,\text{mm/s}$. The results reported in Fig. 10 correspond to $v = 0.025\,\text{mm/s}$.

The above set of parameters (see Table 2), notably the transformation stretch (74), is used in the subsequent studies. However, for completeness, the simulation has additionally been carried out for the trans-

Table 2: Material parameters: compression of a micro-pillar.

Transformation stretch	Elastic constants and chemical energy					Phase-field constants			
λ	c_{11}	c_{44}	c_{12}	F_1^0	F_2^0	γ_{tw}	ℓ	L	f_{c}
0.97	142 GPa	96 GPa	126 GPa	0	3 MPa	0.2 J/m^2	30 nm	0.1 (Pa s)$^{-1}$	0, 1.2 MPa

formation stretch $\mathbf{U}_2$ corresponding to a single (untwinned) variant of the monoclinic β_1' phase in CuAlNi, see Hane (1999), the remaining parameters being unaltered. The corresponding pseudoelastic response is denoted by the solid green line in Fig. 10. As mentioned above, the inelastic deformation is now much larger than in the case of the adjusted HPV, Eq. (74). At the same time, the force at which the transformation proceeds and the width of the hysteresis loop are much smaller. If the chemical energy is increased to $F_2^0 = 8\,\text{MPa}$ (dashed green line in Fig. 10), the force increases, but the hysteresis width is not visibly affected. These qualitative features can be explained using the popular Schmid criterion that is exploited later in this section.

The deformation pattern, typical for all cases studied in this work, is illustrated in Fig. 11. The snapshots show the distribution of the order parameter (in the deformed configuration) during loading; the evolution is essentially reversed during unloading. A movie showing the complete evolution is provided as a supplementary material accompanying this paper.

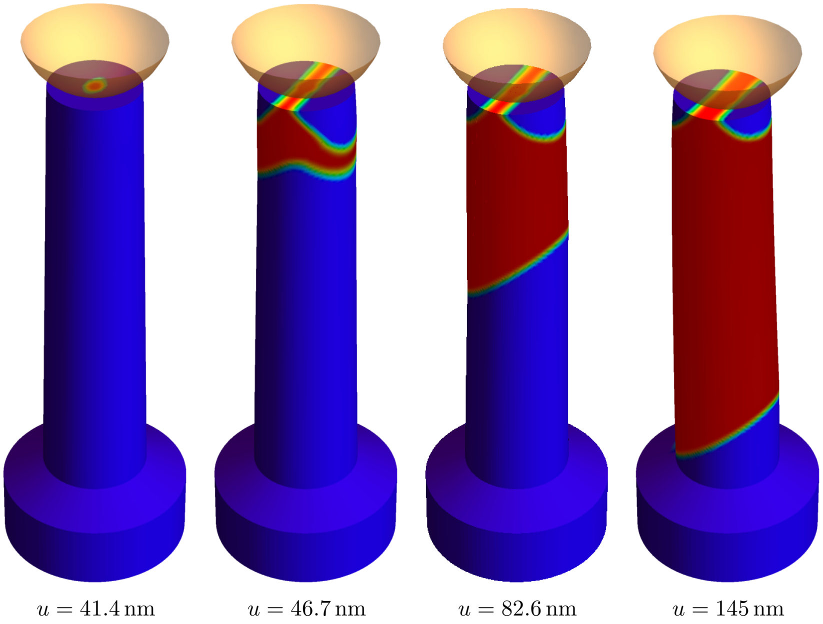

Figure 11: Snapshots of the micro-pillar compression: transformation pattern during loading ($f_{\text{c}} = 1.2\,\text{MPa}$, $v = 0.175\,\text{mm/s}$, $k = +\infty$). Austenite is marked as blue, martensite as red.

The effect of loading rate on the pseudoelastic response predicted for $f_{\text{c}} = 0$ and for $f_{\text{c}} = 1.2\,\text{MPa}$ is shown in Fig. 12. As expected, in the case of the viscous dissipation ($f_{\text{c}} = 0$), the width of the hysteresis loop decreases to zero as the loading rate decreases to zero – except during the initial stage when nucleation of martensite proceeds at a finite speed that is only slightly dependent on the loading rate. When the rate-independent dissipation is included in the model ($f_{\text{c}} = 1.2\,\text{MPa}$), the hysteresis depends to some extent on the loading rate, but its width does not decrease to zero as the loading rate decreases to zero. A quantitative analysis of the related effects is carried out below for a simplified 2D model that is computationally less demanding.

Apart from the width of the hysteresis loop, the pseudoelastic response is similar regardless of the loading rate and the value of f_{c}. An abrupt drop of the load at the initial stage of loading process is associated with

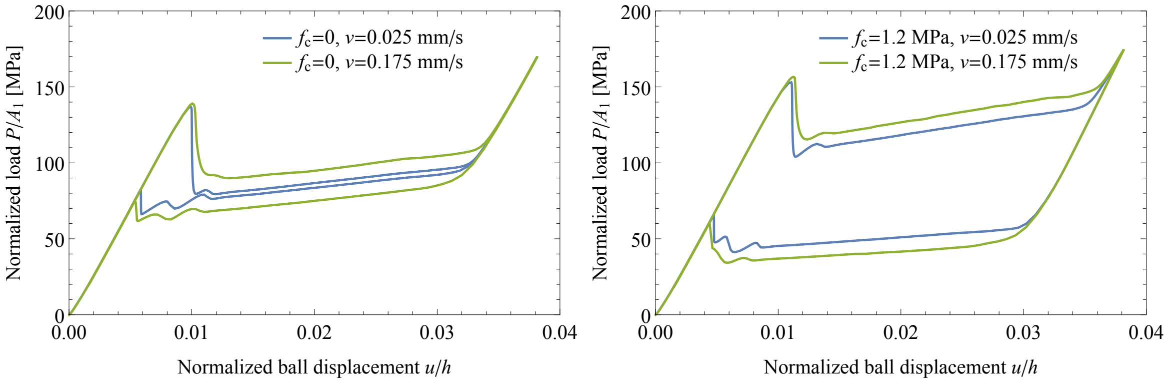

Figure 12: Dependence of the pseudoelastic response on the loading rate for $f_\text{c} = 0$ (left) and $f_\text{c} = 1.2\,\text{MPa}$ (right). The displacement is here normalized by the pillar height h, and the load is normalized by the area at the bottom, $A_1 = \pi R_1^2$.

nucleation of martensite and formation of interfaces. Subsequently, the transformation proceeds through propagation of a single interface, which is quite typical in shape memory alloys (e.g., Shaw and Kyriakides, 1997; Sun and Li, 2002), and this is accompanied here by a gradual increase of the load. The load increases because the cross-section area increases towards the bottom. Once the interface reaches the bottom, the subsequent deformation is predominantly elastic, and thus the stiffness increases. Upon unloading, the interface moves back as the load gradually decreases. Ultimately, the reverse transformation is completed, and annihilation of interfaces is associated with irregular changes of the load. The features discussed above are observed also in the case of the monoclinic martensite, Fig. 10, as well as in the case of the 2D model studied below.

In the 2D model, the plane-strain conditions are assumed, and a single cross-section of the micro-pillar is considered as shown in Fig. 9c. Accordingly, the transformation stretch (74) is redefined to $\mathbf{U}_2 = \text{diag}(1/\lambda, \lambda)$. As the mesh is now finer, the interface thickness parameter ℓ is reduced by the factor of two, so that $\ell = 15\,\text{nm}$, and the mobility parameter L is increased by the factor of two, thus $L = 0.2\,(\text{Pa}\,\text{s})^{-1}$, so that the effective mobility $\hat{L}$ is not affected, cf. Eq. (72). The other material and geometrical parameters remain the same. The finite element mesh employed in 2D simulations is shown in Fig. 9c. Note that the mesh shown in Fig. 9c is four times coarser than the mesh used in the actual computations.

The 2D deformation pattern, shown in Fig. 13, and the respective pseudoelastic response, shown in Fig. 14, are very similar to those of the full 3D model. The visible difference in the elastic stiffness is a well-known effect resulting from the transition from 3D to plane strain while keeping the elastic constants unchanged.

The 2D results will now be used for a quantitative study of the effect of loading rate on dissipation. As the process is assumed isothermal here, the energy dissipated during the complete loading–unloading cycle is equal to the area of the pseudoelastic hysteresis loop,

$$H = \frac{1}{\bar{V}} \oint \bar{P}\,\text{d}u\,, \qquad \bar{V} = (R_1 + R_2)h, \tag{75}$$

where H is the average density of dissipation per unit volume $\bar{V}$ of the micro-pillar. The force $\bar{P}$ and the volume $\bar{V}$ are here referred to the unit thickness in the out-of-plane direction. Figure 15 shows the obtained dependence of the dissipated energy on the loading rate for $f_\text{c} = 0$ and $f_\text{c} = 1.2\,\text{MPa}$. The results of 3D simulations, also included in Fig. 15, are consistent with the 2D results. A simple analytical estimate of H is derived as follows.

The dissipated energy per unit volume swept by an interface propagating with normal speed $v_n > 0$ is equal to the corresponding driving force $\hat{f}$ derived from the dissipation potential (66),

$$\hat{f} = \frac{\partial \hat{D}}{\partial v_n} = \frac{v_n}{\hat{L}} + f_\text{c}, \qquad v_n = \frac{v \cos\varphi}{\varepsilon^\text{t}}, \tag{76}$$

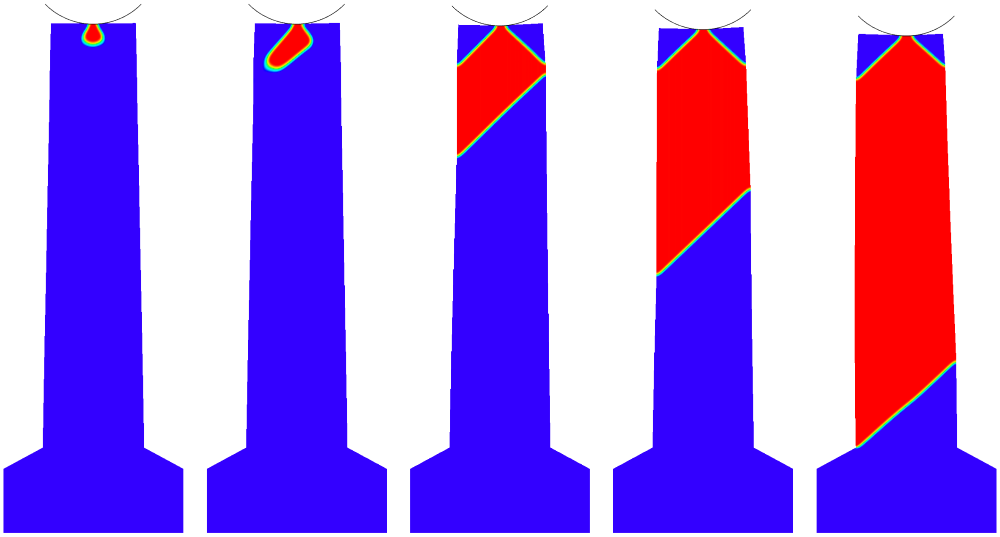

$u = 30.4\,\mathrm{nm}$ $u = 32.8\,\mathrm{nm}$ $u = 46.8\,\mathrm{nm}$ $u = 78.4\,\mathrm{nm}$ $u = 135\,\mathrm{nm}$

Figure 13: Snapshots of the micro-pillar compression (2D model): transformation pattern during loading ($f_\mathrm{c} = 1.2\,\mathrm{MPa}$, $v = 0.175\,\mathrm{mm/s}$). Austenite is marked as blue, martensite as red.

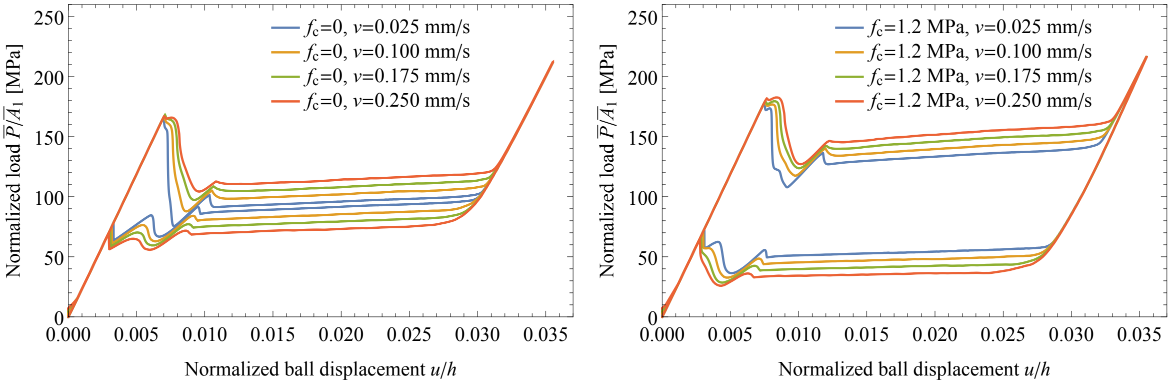

Figure 14: Dependence of the pseudoelastic response on the loading rate for $f_\mathrm{c} = 0$ (left) and $f_\mathrm{c} = 1.2\,\mathrm{MPa}$ (right). The displacement is normalized by the pillar height h, and the load (force per unit thickness) is normalized by the pillar area at the bottom, $\bar{A}_1 = 2R_1$.

where v is the prescribed loading rate, $\varepsilon^\mathrm{t} = 1 - \lambda = 0.03$ is the axial component of the transformation strain, and interface orientation is specified by angle φ, which is close to 45 degrees for the transformation stretch specified by Eq. (74). The energy dissipated during reverse transformation upon unloading is equal to that dissipated during forward transformation (disregarding the nucleation and annihilation processes), thus a theoretical estimate of the energy dissipated during the complete loading–unloading cycle is given by

$$H^* = 2\hat{f} = \frac{2v\cos\varphi}{\hat{L}\varepsilon^\mathrm{t}} + 2f_\mathrm{c}. \tag{77}$$

The above estimate relies on the assumption that the whole volume of the micro-pillar transforms. However, as can be seen in the rightmost snapshot in Fig. 13, this is not exactly so, and some parts of the micro-pillar remain untransformed when the inclined interface reaches the bottom. By introducing an adequate reduction of the volume, the corrected estimate is obtained as follows,

$$H^*_\mathrm{red} = \frac{\bar{V}_\mathrm{red}}{\bar{V}}\,H^*, \qquad \bar{V}_\mathrm{red} = \bar{V} - 2R_1^2 - R_2^2, \tag{78}$$

where, for simplicity, the untransformed regions have been assumed to be right triangles of the sides equal

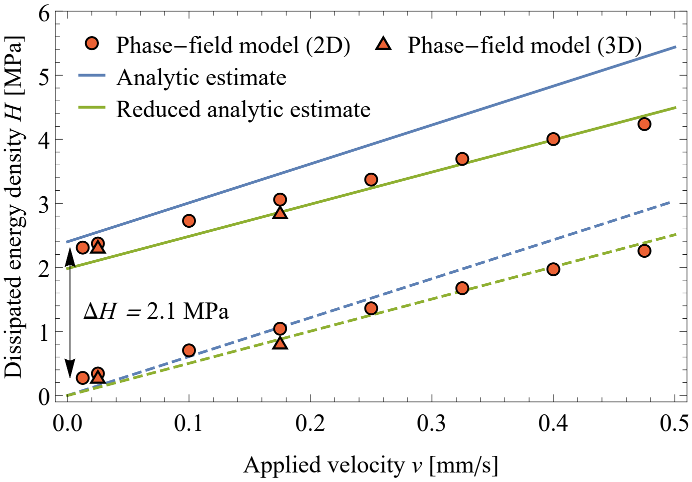

Figure 15: Dependence of the dissipated energy density H on the loading rate. Analytic estimates for the mixed-type and viscous dissipation are denoted by solid and dashed lines, respectively.

to $2R_1$ (the triangle at the bottom) and R_2 (two triangles at the top).

In Fig. 15, the analytical estimates H^* and $H^*_{\rm red}$ of the dissipated energy are compared to the results of phase-field computations. According to the estimate (77), the difference ΔH due to the rate-independent contribution to dissipation is equal to $2f_{\rm c} = 2.4\,$MPa. The actual difference resulting from the phase-field computations is about 2.1 MPa, independent of the loading rate, and this is reasonably well predicted by the corrected estimate (78), which yields 1.98 MPa. Also, the corrected estimate performs better in representing the dependence of the dissipated energy on the loading rate.

It can be seen in Fig. 15 that, for $f_{\rm c} = 0$, the dissipated energy does not decrease exactly to zero as the loading rate vanishes. This is because nucleation of martensite and formation of interfaces, accompanied by an abrupt drop of the load at the initial stage of transformation, is a dynamic process that locally proceeds with a non-zero speed that only weakly depends on the overall loading rate. The energy dissipated during this transient process, even though of viscous origin, can thus be interpreted as a contribution to the overall rate-independent dissipation of the complete system at a slower time scale, cf. Petryk (2005), Petryk and Stupkiewicz (2010) and the references therein. The related effects depend also on the stiffness of the loading device, here assumed infinite, see the discussion below.

Let us estimate the axial stress associated with propagation of the interface. For uniaxial compression, the driving force for propagation of the interface can be estimated as $\hat{f} = -F_2^0 + \sigma\varepsilon^{\rm t}$, where $\varepsilon^{\rm t} = 0.03$ is the axial transformation strain, σ denotes the compressive axial stress (assumed positive here), and F_2^0 is the chemical energy. By equating the driving force with the resistance to transformation resulting from the dissipation potential, cf. Eq. (76), the following expression is obtained

$$\sigma^{\pm} = \frac{1}{\varepsilon^{\rm t}}\Big(F_2^0 \pm \frac{v\cos\varphi}{\hat{L}\varepsilon^{\rm t}} \pm f_{\rm c}\Big), \tag{79}$$

where '$+$' and '$-$' correspond, respectively, to the forward and reverse transformation, i.e. to loading and unloading. In Fig. 16, the above estimate is compared to the phase-field results. The latter are evaluated at the instant when the interface is located in the middle of the micro-pillar. The corresponding stress is obtained by dividing the force by the area in the middle, $\sigma^{\pm} = \bar{P}^{\pm}/(R_1 + R_2)$. A good agreement between the stress estimates obtained in different ways is apparent.

The results discussed above correspond to the case of the loading device of an infinite stiffness so that the displacement of the ball is controlled directly, e.g., by prescribing its (constant) velocity. For a finite stiffness of the loading device, as encountered in practice, the elastic energy accumulated in the loading device is released during the load drop at the initial stage of transformation, and this influences the response. Additional simulations have been performed to illustrate this effect. Specifically, the position of the ball has

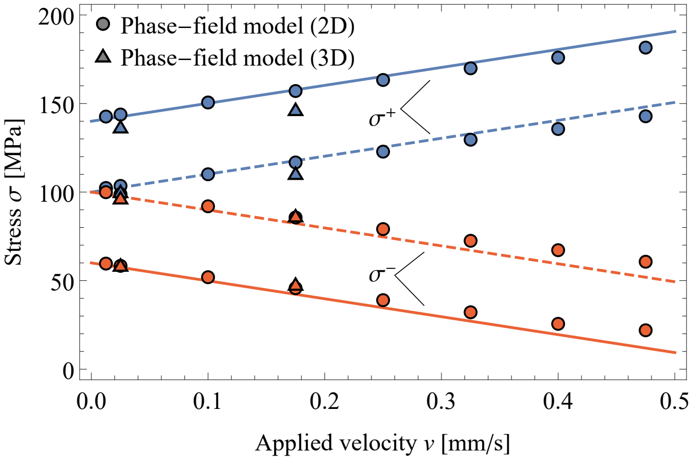

Figure 16: Dependence of the transformation stress $\sigma^\pm$ on the loading rate: finite-element results (markers) and analytic estimate, Eq. (79), for the mixed-type dissipation (solid lines) and viscous dissipation (dashed lines).

been controlled through a linear spring of stiffness $\bar{k}$ (related to unit thickness in the out-of-plane direction) representing the lumped elastic response of the loading device.

Figure 17 shows the obtained pseudoelastic response for three selected values of $\bar{k}$. In all cases, the linear spring was loaded by applying a constant velocity $v = 0.175\,\text{mm/s}$. For a very high value of $\bar{k} = 10^5\ (\text{N/m})/\mu\text{m} = 100\,\text{GPa}$, the response is similar to that reported earlier for the infinitely stiff device. As the stiffness is decreased, the softening branch that corresponds to the transient nucleation event spans a larger fraction of the loading curve. In the case of viscous dissipation, $f_\text{c} = 0$, for $\bar{k} = 1\,\text{GPa}$ the nucleation event triggers transformation in the whole micro-pillar, and no steady-state propagation of the interface is observed. The stiffness influences also the last stage of unloading, but the effect on the load–displacement response is significantly less pronounced.

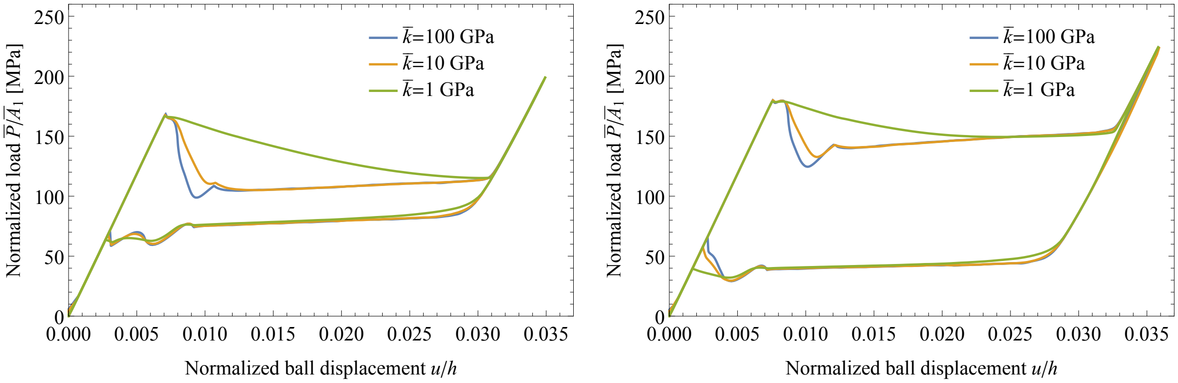

Figure 17: Effect of the stiffness $\bar{k}$ of the loading device on the pseudoelastic response for $f_\text{c} = 0$ (left) and $f_\text{c} = 1.2\,\text{MPa}$ (right).

Qualitatively, the response predicted for $\bar{k} = 1\,\text{GPa}$, and also the response predicted by the 3D model using the stiffness $k = 200\,\text{N/m}$, are similar to the experiment of San Juan et al. (2009), see Fig. 10. In fact, in the experiment, the duration of the process corresponding to the softening branch of the loading curve was only 2 ms (San Juan et al., 2009). This suggests that, once martensite was nucleated, the transformation was triggered in the whole micro-pillar in a dynamic fashion, which can be described by the present model by adequately adjusting the stiffness of the loading device.

5. Conclusion

The phase-field framework for modelling of twinning and martensitic transformations has been extended by including rate-independent dissipation. This has been achieved, apparently for the first time, by introducing into this framework a non-smooth mixed-type dissipation potential that combines viscous and rate-independent contributions. As a result, the interface motion, and microstructure evolution in general, is triggered only when the thermodynamic driving force exceeds a finite threshold, in contrast to the case of purely viscous dissipation which is the basis of all available phase-field models of microstructure evolution. New qualitative effects have been thus introduced into phase-field modelling, such as arrest of microstructure in a state of non-vanishing driving forces, and finite and controllable hysteresis in a closed cycle at a vanishing loading rate. These effects, illustrated here by representative finite-element computations, constitute essential features of the experimentally observed response of materials undergoing displacive transformations such as twinning and martensitic transformation.

The evolution problem, both in the rate and in the finite-step incremental form, has been formulated within a non-smooth variational framework for minimization of the total incremental energy, including free energy and dissipation increments. Computational treatment, which has lead to an efficient finite-element formulation, relies on a specific version of the augmented Lagrangian technique in which the dissipation potential vertex and the bound constraints on the order parameter are handled by a single Lagrange multiplier field. Remarkably, the initially non-smooth minimization problem has been converted in this way into a smooth stationarity problem that can be conveniently solved using the Newton method. It is an open problem how to extend this computational approach to systems with more than two phases.

Acknowledgement. This work has been partially supported by the National Science Center (NCN) in Poland through Grant No. 2015/17/B/ST8/03242. KT has also been supported by the Charles University Research Program No. UNCE/SCI/023.

Appendix A. Equilibrium profile of the interface for the double-obstacle potential

The interfacial part F_Γ of the free energy F represents the energy of *diffuse* interfaces, and F_Γ is thus the energy density per unit reference *volume*. In order to interpret the factor γ in Eq. (23) as the interfacial energy density per unit reference *area*, the term in the parentheses in Eq. (23) must represent the measure of the area of the diffuse interface. Accordingly, neglecting the influence of the bulk energy F_B on the profile of the diffuse interface, which corresponds to minimization of the interfacial energy alone, the following property must hold for a single planar interface with ξ denoting the coordinate in the direction normal to the interface,

$$\inf_{\substack{\eta\in\mathcal{W},\ 0\leq\eta\leq 1,\\ \eta(-\infty)=0,\ \eta(+\infty)=1}} \int_{-\infty}^{+\infty} \left(\frac{4\ell}{\pi} \left| \frac{\mathrm{d}\eta}{\mathrm{d}\xi} \right|^2 + \frac{4}{\pi\ell}\eta(1-\eta) \right) \mathrm{d}\xi = 1. \tag{A.1}$$

Throughout this paper we assume that a function space, like $\mathcal{W}$ in Eq. (A.1), is suitable for performing the underlying mathematical operations without specifying it explicitly. For instance, $\mathcal{W}$ in Eq. (A.1) can be the Sobolev space $W^{1,2}$ containing real functions which are square-integrable together with their first derivative.

Solution of the minimization problem (A.1) is obtained by constructing the following Lagrange functional $\mathcal{L}$,

$$\mathcal{L}[\eta,\lambda_0,\lambda_1] = \int_{-\infty}^{+\infty} \left(\frac{4\ell}{\pi} \left| \frac{\mathrm{d}\eta}{\mathrm{d}\xi} \right|^2 + \frac{4}{\pi\ell}\eta(1-\eta) - \eta\lambda_0 - (1-\eta)\lambda_1 \right) \mathrm{d}\xi, \tag{A.2}$$

where λ_0 and λ_1 are the Lagrange multipliers that are used to enforce the inequality constraints $\eta \geq 0$ and $\eta \leq 1$, respectively. The function $\eta(\cdot)$ that renders $\mathcal{L}$ stationary satisfies the following Euler–Lagrange equation,

$$\frac{8\ell}{\pi}\frac{\mathrm{d}^2\eta}{\mathrm{d}\xi^2} - \frac{4}{\pi\ell}(1-2\eta) + \lambda_0 - \lambda_1 = 0, \tag{A.3}$$

except at the boundary of the diffuse interface, where $\mathrm{d}^2\eta/\mathrm{d}\xi^2$ is discontinuous. The standard Kuhn–Tucker conditions are also imposed:

$$\eta \geq 0, \quad \lambda_0 \ \geq 0, \quad \eta\lambda_0 = 0 \qquad \text{and} \qquad 1-\eta \geq 0, \quad \lambda_1 \ \geq 0, \quad (1-\eta)\lambda_1 = 0. \tag{A.4}$$

Solution of the Euler–Lagrange equation (A.3), with an additional condition $\eta(\varsigma) = \frac{1}{2}$ that prescribes the position of the interface at $\xi = \varsigma$, yields the following profile of the diffuse interface

$$\eta(\xi) = \begin{cases} 0 & \text{if } \ \xi < \varsigma - \pi\ell/2, \\ \dfrac{1}{2}\Big(1 + \sin\Big(\dfrac{\xi-\varsigma}{\ell}\Big)\Big) & \text{if } \ \varsigma - \pi\ell/2 \leq \xi \leq \varsigma + \pi\ell/2, \\ 1 & \text{if } \ \varsigma + \pi\ell/2 < \xi. \end{cases} \tag{A.5}$$

The thickness of the diffuse interface is thus equal to $\pi\ell$. It can be checked that the integral in Eq. (A.1) is indeed equal to unity for $\eta(\xi)$ specified by Eq. (A.5).

Appendix B. Proof of conditional convexity of $\boldsymbol{\Pi}^{\mathrm{v}}_{\boldsymbol{\tau}}[\mathbf{u},\cdot]$

The condition for convexity of a smooth functional $\Pi^{\mathrm{v}}_{\tau}[\mathbf{u},\cdot]$ over a convex set $\omega \subset \mathcal{W}_\eta$ is adopted in the form

$$\delta_{\bar{\eta}}\Pi^{\mathrm{v}}_{\tau}[\mathbf{u},\bar{\eta}] - \delta_{\eta}\Pi^{\mathrm{v}}_{\tau}[\mathbf{u},\eta] \geq 0 \quad \forall \bar{\eta},\eta \in \omega \ \text{ with } \ \delta\bar{\eta} = \delta\eta = \bar{\eta} - \eta\,. \tag{B.1}$$

The Gateaux differential $\delta_{\eta}\Pi^{\mathrm{v}}_{\tau}[\mathbf{u},\eta]$ is given by expression (40). The free energy density $F(\nabla\mathbf{u},\eta,\nabla\eta)$ depends on $\nabla\eta$ only through Eq. (23), from which it follows that the partial derivative

$$\frac{\partial F(\nabla\mathbf{u},\eta,\nabla\eta)}{\partial\nabla\eta} = \gamma\frac{8\ell}{\pi}\nabla\eta \tag{B.2}$$

is independent of η. Denote by $\breve{f}(\nabla\mathbf{u},\eta) = -\partial F/\partial\eta$ the part of f that is independent of $\nabla\eta$. On substituting formula (40) and using the above expressions along with the quadratic potential D^{v} defined by Eq. (2), inequality (B.1) takes the form

$$\int_B \left(\left(\breve{f}(\nabla\mathbf{u},\eta) - \breve{f}(\nabla\mathbf{u},\bar{\eta}) + \frac{\bar{\eta}-\eta}{\tau L}\right)(\bar{\eta}-\eta) + \gamma\frac{8\ell}{\pi}|\nabla\bar{\eta} - \nabla\eta|^2\right)\mathrm{d}\mathbf{X} \geq 0 \quad \forall\eta,\bar{\eta}\in\omega\,. \tag{B.3}$$

Since the dependence of $\breve{f}$ on η is continuously differentiable (although highly nonlinear), it follows that $\breve{f}(\nabla\mathbf{u},\cdot)$ is Lipschitz continuous over a bounded interval $[0,1]$, i.e. there exists a real constant $K > 0$ such that

$$|\breve{f}(\nabla\mathbf{u},\eta) - \breve{f}(\nabla\mathbf{u},\bar{\eta})| \leq K\,|\bar{\eta}-\eta| \qquad \forall\bar{\eta},\eta\in[0,1]\,. \tag{B.4}$$

It is concluded that the convexity condition (B.3) is satisfied for a given field of displacements $\mathbf{u}$ if

$$\tau < \frac{1}{LK} \qquad \text{and} \qquad \omega = \{\eta\in\mathcal{W}_\eta \mid 0\leq\eta\leq 1\}\,. \tag{B.5}$$

Hence, if Eq. (B.5) holds then $\Pi^{\mathrm{v}}_{\tau}[\mathbf{u},\cdot]$ is convex over the above $\omega\subset\mathcal{W}_\eta$. □

References

Abeyaratne, R., Chu, C., James, R. D., 1996. Kinetics of materials with wiggly energies: theory and application to the evolution of twinning microstructures in a Cu–Al–Ni shape memory alloy. Phil. Mag. A 73, 457–497.

Abeyaratne, R., Knowles, J. K., 1991. Kinetic relations and the propagation of phase boundaries in solids. Arch. Ration. Mech. Anal. 114, 119–154.

Abeyaratne, R., Knowles, J. K., 1997. On the kinetics of an austenite→martensite phase transformation induced by impact in a Cu–Al–Ni shape-memory alloy. Acta Mater. 45, 1671–1683.

Ahluvalia, R., Lookman, T., Saxena, A., Albers, R. C., 2004. Landau theory for shape memory polycrystals. Acta Mater. 52, 209–218.

Ammar, K., Appolaire, B., Cailletaud, G., Forest, S., 2009. Combining phase field approach and homogenization methods for modelling phase transformation in elastoplastic media. Eur. J. Comp. Mech. 18, 485–523.

Artemev, A., Wang, Y., Khachaturyan, A. G., 2000. Three-dimensional phase field model and simulation of martensitic transformation in multilayer systems under applied stresses. Acta Mater. 48, 2503–2518.

Auricchio, F., Taylor, R. L., 1997. Shape-memory alloys: modelling and numerical simulations of finite-strain superelastic behavior. Comp. Meth. Appl. Mech. Engng. 143, 175–194.

Bartel, T., Menzel, A., 2016. Modelling and simulation of cyclic thermomechanical behaviour of NiTi wires using a weak discontinuity approach. Int. J. Fract. 202, 281–293.

Bertsekas, D. P., 1996. Constrained Optimization and Lagrange Multiplier Methods, 2nd Edition. Athena Scientific, Belmont, MA.

Bhattacharya, K., 1999. Phase boundary propagation in a heterogeneous body. Proc. R. Soc. Lond. A 455, 757–766.

Bhattacharya, K., 2003. Microstructure of martensite: why it forms and how it gives rise to the shape-memory effect. Oxford University Press, Oxford.

Chen, L. Q., 2002. Phase-field models for microstructure evolution. Annu. Rev. Mater. Res. 32, 113–140.

Chen, L. Q., Shen, J., 1998. Applications of semi-implicit Fourier-spectral method to phase field equations. Comp. Phys. Comm. 108, 147–158.

Chu, C., 1993. Hysteresis and microstructures: a study of biaxial loading on compound twins of copper-aluminum-nickel single crystals. Ph.D. thesis, University of Minnesota.

Clayton, J. D., Knap, J., 2011. A phase field model of deformation twinning: Nonlinear theory and numerical simulations. Physica D 240, 841–858.

Fischer, F. D., Svoboda, J., Petryk, H., 2014. Thermodynamic extremal principles for irreversible processes in materials science. Acta Mater. 67, 1–20.

Hackl, K., Heinen, R., 2008. A micromechanical model for pretextured polycrystalline shape-memory alloys including elastic anisotropy. Continuum Mech. Thermodyn. 19, 499–510.

Halphen, B., Nguyen, Q. S., 1975. Sur les matériaux standard généralisés. Journal de Mécanique 14, 39–63.

Hane, K. F., 1999. Bulk and thin film microstructures in untwinned martensites. J. Mech. Phys. Solids 47, 1917–1939.

Helm, D., Haupt, P., 2003. Shape memory behaviour: modelling within continuum thermomechanics. Int. J. Sol. Struct. 40, 827–849.

Hildebrand, F. E., Miehe, C., 2012. A phase field model for the formation and evolution of martensitic laminate microstructure at finite strains. Phil. Mag. 92, 4250–4290.

Hudobivnik, B., Korelc, J., 2016. Closed-form representation of matrix functions in the formulation of nonlinear material models. Finite Elem. Anal. Design 111, 19–32.

Idesman, A. V., Levitas, V. I., Preston, D. L., Cho, J. Y., 2005. Finite element simulations of martensitic phase transitions and microstructures based on a strain softening model. J. Mech. Phys. Solids 53, 495–523.

Korelc, J., 2002. Multi-language and multi-environment generation of nonlinear finite element codes. Engineering with Computers 18, 312–327.

Korelc, J., 2009. Automation of primal and sensitivity analysis of transient coupled problems. Comp. Mech. 44, 631–649.

Korelc, J., Stupkiewicz, S., 2014. Closed-form matrix exponential and its application in finite-strain plasticity. Int. J. Num. Meth. Engng. 98, 960–987.

Kružík, M., Mielke, A., Roubíček, T., 2005. Modelling of microstructure and its evolution in shape-memory-alloy single-crystals, in particular in CuAlNi. Meccanica 40, 389–418.

Lahellec, N., Suquet, P., 2007. On the effective behavior of nonlinear inelastic composites: I. Incremental variational principles. J. Mech. Phys. Solids 55, 1932–1963.

Lengiewicz, J., Wichrowski, M., Stupkiewicz, S., 2014. Mixed formulation and finite element treatment of the mass-conserving cavitation model. Tribol. Int. 72, 143–155.

Levitas, V. I., Lee, D.-W., 2007. Athermal resistance to interface motion in the phase-field theory of microstructure evolution. Phys. Rev. Lett. 99, 245701.

Levitas, V. I., Lee, D.-W., Preston, D. L., 2010. Interface propagation and microstructure evolution in phase field models of stress-induced martensitic phase transformations. Int. J. Plasticity 26 (3), 395–422.

Levitas, V. I., Levin, V. A., Zingerman, K. M., Freiman, E. I., 2009. Displacive phase transitions at large strains: phase-field theory and simulations. Phys. Rev. Lett. 103, 025702.

Levitas, V. I., Preston, D. L., 2002. Three-dimensional Landau theory for multivariant stress-induced martensitic phase transformations. I. Austenite↔martensite. Phys. Rev. B 66, 134206.

Mamivand, M., Zaeem, M. A., El Kadiri, H., 2013. A review on phase field modeling of martensitic phase transformation. Comput. Mater. Sci. 77, 304–311.

Miehe, C., Hofacker, M., Welschinger, F., 2010. A phase field model for rate-independent crack propagation: Robust algorithmic implementation based on operator splits. Comp. Meth. Appl. Mech. Engng. 199, 2765–2778.

Mielke, A., Roubíček, T., 2015. Rate-independent Systems. Springer, New York.

Moelans, N., Blanpain, B., Wollants, P., 2008. An introduction to phase-field modeling of microstructure evolution. Calphad 32, 268–294.

Moreau, J., 1974. On unilateral constraints, friction and plasticity. In: Capriz, G., Stampacchia, G. (Eds.), New Variational Techniques in Mathematical Physics. CIME, Edizioni Cremonese, Roma, pp. 175–322.

Moreau, J. J., 1970. Sur les lois de frottement, de plasticité et de viscosité. C. R. Acad. Sci. Paris, A 271, 608–611.

Mosler, J., Shchyglo, O., Hojjat, H. M., 2014. A novel homogenization method for phase field approaches based on partial rank-one relaxation. J. Mech. Phys. Solids 68, 251–266.

Ngan, S. C., Truskinovsky, L., 1999. Thermal trapping and kinetics of martensitic phase boundaries. J. Mech. Phys. Solids 47, 141–172.

Onsager, L., 1931. Reciprocal relations in irreversible processes. I. Phys. Rev. 37, 405–426.

Otsuka, K., Wayman, C. M. (Eds.), 1998. Shape Memory Materials. Cambridge University Press.

Penrose, O., Fife, P. C., 1990. Thermodynamically consistent models of phase-field type for the kinetics of phase transitions. Physica D 43, 44–62.

Petryk, H., 2005. Thermodynamic conditions for stability in materials with rate-independent dissipation. Phil. Trans. R. Soc. Lond. A 363, 2479–2515.

Petryk, H., Stupkiewicz, S., 2010. Interfacial energy and dissipation in martensitic phase transformations. Part I: Theory. J. Mech. Phys. Solids 58, 390–408.

Petryk, H., Stupkiewicz, S., Maciejewski, G., 2010. Interfacial energy and dissipation in martensitic phase transformations. Part II: Size effects in pseudoelasticity. J. Mech. Phys. Solids 58, 373–389.

Peypouquet, J., 2015. Convex Optimization in Normed Spaces. Springer International Publishing.

Puglisi, G., Truskinovsky, L., 2002. Rate independent hysteresis in a bi-stable chain. J. Mech. Phys. Solids 50, 165–187.

Raniecki, B., Lexcellent, C., 1994. R_L-models of pseudoelasticity and their specifications for some shape memory alloys. Eur. J. Mech. A/Solids 13, 21–50.

Raous, M., Cangemi, L., Cocu, M., 1999. A consistent model coupling adhesion, friction, and unilateral contact. Comp. Meth. Appl. Mech. Engng. 177, 383–399.

Reese, S., Christ, D., 2008. Finite deformation pseudo-elasticity of shape memory alloys – Constitutive modelling and finite element implementation. Int. J. Plasticity 24, 455–482.

Rice, J. R., 1975. Continuum mechanics and thermodynamics of plasticity in relation to microscale deformation mechanisms. In: Argon, A. S. (Ed.), Constitutive Equations in Plasticity. MIT Press, Cambridge, Mass., pp. 23–79.

Rockafellar, R. T., 1970. Convex Analysis. Princeton University Press, Princeton.

Roubíček, T., 2011. Approximation in multiscale modelling of microstructure evolution in shape-memory alloys. Continuum Mech. Thermodyn. 23, 491–507.

Sadjadpour, A., Bhattacharya, K., 2007. A micromechanics inspired constitutive model for shape-memory alloys. Smart Mater. Struct. 16, 1751–1765.

San Juan, J., Nó, M. L., Schuh, C. A., 2009. Nanoscale shape-memory alloys for ultrahigh mechanical damping. Nature Nanotechnology 4, 415–419.

Schneider, D., Tschukin, O., Choudhury, A., Selzer, M., Boehlke, T., Nestler, B., 2015. Phase-field elasticity model based on mechanical jump conditions. Comp. Mech. 55, 887–901.

Sedlák, P., Frost, M., Benešová, B., Ben Zineb, T. Šittner, P., 2012. Thermomechanical model for NiTi-based shape memory alloys including R-phase and material anisotropy under multi-axial loadings. Int. J. Plasticity 39, 132–151.

Shaw, J. A., Kyriakides, S., 1997. On the nucleation and propagation of phase transformation fronts in a NiTi alloy. Acta Mater. 45, 683–700.

Souza, A. C., Mamiya, E. N., Zouain, N., 1998. Three-dimensional model for solids undergoing stress-induced phase transformations. Eur. J. Mech. A/Solids 17, 789–806.

Steinbach, I., 2009. Phase-field models in materials science. Modelling Simul. Mater. Sci. Eng. 17, 073001.

Steinbach, I., Pezzola, F., Nestler, B., Seesselberg, M., Prieler, R., Schmitz, G. J., Rezende, J. L. L., 1996. A phase field concept for multiphase systems. Physica D 94, 135–147.

Stupkiewicz, S., Petryk, H., 2002. Modelling of laminated microstructures in stress-induced martensitic transformation. J. Mech. Phys. Solids 50, 2303–2331.

Stupkiewicz, S., Petryk, H., 2013. A robust model of pseudoelasticity in shape memory alloys. Int. J. Num. Meth. Engng. 93, 747–769.

Suezawa, M., Sumino, K., 1976. Behaviour of elastic constants in Cu-Al-Ni alloy in the close vicinity of M_s-point. Scripta Metall. 10, 789–792.

Sun, Q. P., Li, Z. Q., 2002. Phase transformation in superelastic NiTi polycrystalline micro-tubes under tension and torsion—from localization to homogeneous deformation. Int. J. Sol. Struct. 39, 3797–3809.

Thamburaja, P., Anand, L., 2001. Polycrystalline shape-memory materials: effect of crystallographic texture. J. Mech. Phys. Solids 49, 709–737.

Tůma, K., Stupkiewicz, S., 2016. Phase-field study of size-dependent morphology of austenite-twinned martensite interface in CuAlNi. Int. J. Solids Struct. 97–98, 89–100.

Tůma, K., Stupkiewicz, S., Petryk, H., 2016. Size effects in martensitic microstructures: finite-strain phase field model versus sharp-interface approach. J. Mech. Phys. Solids 95, 284–307.

Šittner, P., Novák, V., 2000. Anisotropy of martensitic transformations in modeling of shape memory alloy polycrystals. Int. J. Plasticity 16, 1243–1268.

Wang, Y., Khachaturyan, A. G., 1997. Three-dimensional field model and computer modeling of martensitic transformations. Acta Mater. 45, 759–773.

Wang, Y., Li, J., 2010. Phase field modeling of defects and deformation. Acta Mater. 58, 1212–1235.

Yasunaga, M., Funatsu, Y., Kojima, S., Otsuka, K., Suzuki, T., 1983. Measurement of elastic constants. Scripta Metall. 17, 1091–1094.

Zhang, Z., James, R. D., Muller, S., 2009. Energy barriers and hysteresis in martensitic phase transformations. Acta Mater. 57, 4332–4352.

Ziegler, H., 1963. Some extremum principles in irreversible thermodynamics with application to continuum mechanics. In: Progress in Solid Mechanics, Vol. IV. North-Holland, Amsterdam, pp. 91–193.